# The Folding Pathway of an Ig Domain is Conserved On and Off the Ribosome

Pengfei Tian[1‡], Annette Steward[2‡], Renuka Kudva[3‡], Ting Su[5‡], Patrick J. Shilling[3], Adrian A. Nickson[2], Jeffrey J. Hollins[2], Roland Beckmann[5], Gunnar von Heijne[3,4#], Jane Clarke[2#] and Robert B. Best[1#]

[1]Laboratory of Chemical Physics, NIDDK, National Institutes of Health, 5 Memorial Drive, Bethesda, MD 20892-0520, USA.

[2]Department of Chemistry, University of Cambridge, Lensfield Road, Cambridge, CB2 1EW, UK.

[3]Department of Biochemistry and Biophysics, Stockholm University, SE-10691 Stockholm, Sweden.

[4]Science for Life Laboratory Stockholm University, Box 1031, SE-171 21 Solna, Sweden.

[5]Gene Center, Department of Biochemistry and Center for Integrated Protein Science Munich, CiPS-M, Feodor-Lynen-Strasse 25, Ludwig Maximilian University of Munich, 81377 Munich, Germany.

[‡]P.T., A.S., R.K. and T.S. contributed equally to this work.

[#]Corresponding authors

Classification: Biological Sciences, Biophysics and Computational Biology

**Abstract**

Proteins that fold cotranslationally may do so in a restricted configurational space, due to the volume occupied by the ribosome. How does this environment, coupled with the close proximity of the ribosome, affect the folding pathway of a protein? Previous studies have shown that the cotranslational folding process for many proteins, including small, single domains, is directly affected by the ribosome. Here, we investigate the cotranslational folding of an all-β immunoglobulin domain, titin I27. Using an arrest peptide-based assay and structural studies by cryo-EM, we show that I27 folds in the mouth of the ribosome exit tunnel. Simulations that use a kinetic model for the force-dependence of escape from arrest, accurately predict the fraction of folded protein as a function of length. We used these simulations to probe the folding pathway on and off the ribosome. Our simulations - which also reproduce experiments on mutant forms of I27 - show that I27 folds, while still sequestered in the mouth of the ribosome exit tunnel, by essentially the same pathway as free I27, with only subtle shifts of critical contacts from the C to the N terminus.

**Significance Statement**

Most proteins need to fold into a specific three-dimensional structure in order to function. The mechanism by which isolated proteins fold has been thoroughly studied by experiment and theory. However, in the cell proteins do not fold in isolation, but are synthesized as linear chains by the ribosome during translation. It is therefore natural to ask at which point during synthesis proteins fold, and whether this differs from the folding of isolated protein molecules. By studying folding of a well characterized protein domain, titin I27, stalled at different points during translation, we show that it already folds in the mouth of the ribosome exit tunnel, and that the mechanism is almost identical to that of the isolated protein.

## Introduction

To what extent is the cotranslational folding pathway of a protein influenced by the presence of the ribosome and by the vectorial emergence of the polypeptide chain during translation? Recent studies have shown that small proteins can fold inside the ribosome exit tunnel (e.g., the small zinc finger domain ADR1a) (1), while other proteins can fold at the mouth of the tunnel (e.g., the three-helix bundle spectrin domains) (2); however some proteins may be simply too large to fold within the confines of the ribosome (e.g., DHFR) (3). The nature of cotranslational protein folding is determined by a number of biophysical factors, including the folding properties of the isolated protein (4-9), together with the effects the ribosome itself may have on the folding process (10-16). Due to the spatial constraints imposed upon the nascent chain by the confines of the tunnel, and effects due to the close proximity of the ribosome itself, the ribosome has been shown to influence directly the cotranslational folding of small proteins and single domains: The stability of folded or partly folded states may be reduced when folding occurs close to, or within the confines of, the ribosome (17, 18); the folding kinetics are expected to be correspondingly altered, with the rate of folding likely to be decreased and the unfolding rate increased, in close proximity to the ribosome(18). Interactions of the folded state or nascent polypeptide with the ribosome may also be either stabilising or destabilising (19, 20). Since translation is vectorial in nature, it is possible that when proteins fold cotranslationally they fold via different pathways than those used when proteins fold outside the ribosome, or when isolated proteins fold *in vitro* (2, 11, 21-24). However, addressing these issues is challenging, because standard protein folding methods are not directly applicable to cotranslational folding.

The folding of the protein close to the ribosome generates a pulling force on the nascent chain. This force has been probed by single molecule (25) as well as arrest peptide (AP) experiments (1-3). In this work, we use such arrest peptide-based cotranslational force-measurement experiments, simulations, and structural studies to investigate how the ribosome affects the folding of titin I27, a small all-β immunoglobulin domain with a complex greek-key fold; the stability, kinetics and folding pathway of I27 has been extensively characterized in previous studies of the isolated domain (26, 27). In this study we investigate whether I27 can begin to fold in the confines of the ribosome, and if the folding pathway observed in the isolated domain is conserved during cotranslational folding. Results from all three techniques show that I27 folds in the mouth of the ribosome exit tunnel; our simulations correctly capture the onset of folding in I27 and three mutant variants, allowing

us to predict how destabilisation of regions that fold early and late in the isolated domain affect folding on the ribosome. Our simulations further show that the folding pathway of I27 is largely unaffected by the presence of the ribosome, except for small but significant changes observed for contacts near the N and C termini.

## Results

### I27 folds close to the ribosome

In order to gain insight into when I27 can commence folding on the ribosome, we employed an arrest peptide force-measurement assay (28) carried out using the PURE *in vitro* translation system, as described in (1-3). In these experiments, the *E. coli* SecM arrest peptide (AP) is used to stall the nascent protein chain temporarily during translation. The yield of full-length protein which escapes stalling in a defined time interval ($f_{FL}$), determined from SDS-PAGE gels, provides a proxy for the pulling force exerted on the nascent chain by the protein as it folds (1-3) (Figure 1A). By measuring $f_{FL}$ for a set of constructs where the length $L$ of the linker between the target protein and the SecM AP is systematically varied, a force profile can be recorded that reflects the points during translation where the folding process starts and ends. Previous work has shown that the location of the main peak in a force profile correlates with the acquisition of protease resistance in an on-ribosome pulse-proteolysis assay (17, 29) and that the amplitude of the main force peak correlates with the thermodynamic stability of the protein (29, 30), indicating that the main peak represents a *bona fide* folding event rather than, *e.g.*, the formation of a molten globule. The sharp onset of the main force peak observed for most proteins analysed thus far (29) is also as expected for a cooperative folding event.

The force profile for wild-type I27 (Figure 1B) has a distinct peak at $L$ = 35-38 residues (see Methods for sequences of the constructs). This peak is absent from the force profile for the mutant I27[W34E], a non-folding variant of I27, demonstrating that the peak is due to a folding event and not, for example, to non-specific interactions of the unfolded nascent chain with the ribosome. The non-zero $f_{FL}$ for the non-folding mutant is attributed to the spontaneous rate of escape from arrest in the absence of acceleration by forces associated with folding. Since it takes ~35 residues in an extended conformation to span the ~100 Å long exit tunnel (31), the critical length $L \approx 35$ residues suggests that I27 starts folding while in mouth of the exit tunnel.

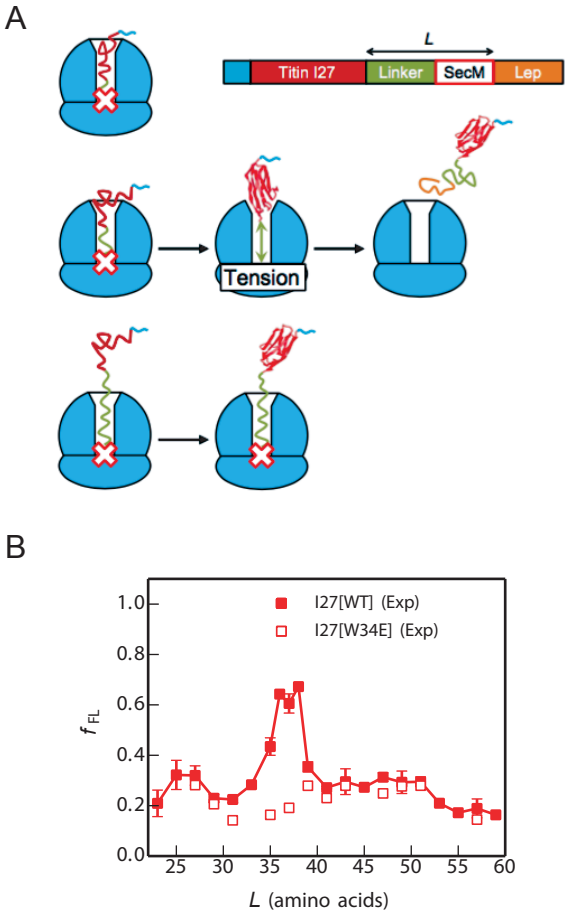


**Figure 1**. Cotranslational folding of the titin I27 domain by force-profile analysis. (A) The force-measurement assay (modified from (2)). I27, preceded by a His-tag, is placed *L* residues away from the last amino acid of the SecM AP, which in turn is followed by a 23-residue C-terminal tail derived from *E. coli* LepB. Constructs are translated for 15 min. in the PURE *in vitro* translation system, and the relative amounts of arrested and full-length peptide chains produced are determined by SDS-PAGE. The fraction full-length protein, $f_{FL}$, reflects the force exerted on the AP by the folding of I27 at linker length *L*. At short linker lengths (top), there is not enough room in the exit tunnel for I27 to fold, little force is exerted on the AP, and the ribosome stalls efficiently on the AP ($f_{FL} \approx 0$). At intermediate linker lengths (middle), there is enough room for I27 to fold but only if the linker segment is stretched, force is exerted on the AP, and stalling is reduced ($f_{FL} > 0$). At long linker lengths (bottom), I27 has already folded when the ribosome reaches the last codon in the AP, and again little force is exerted on the AP ($f_{FL} \approx 0$). (B) Force profiles for the I27 domain (solid squares) and the non-folding (nf) mutant I27[W34E] (open squares). The standard error of $f_{FL}$ is calculated for values of *L* where three or more experiments were performed.

**Cryo-EM shows that I27 folds in the mouth of the exit tunnel**

To confirm that the peak in the force profile corresponds to the formation of a folded I27 domain, we replaced the SecM AP with the stronger TnaC AP (32-34) and purified stalled ribosome-nascent chain complexes (RNCs) carrying an N-terminally His-tagged I27[*L*=35]

construct (see Methods). The construct was expressed in *E. coli*, RNCs were purified using the N-terminal His-tag, and an RNC structure with an average resolution of 3.2 Å (SI Appendix, Fig. S1) was obtained by cryo-EM. In addition to the density corresponding to the TnaC AP, a well-defined globular density (~4.5-9 Å resolution) was visible protruding from the exit tunnel (Figure 2A). Given the flat ellipsoidal shapes of the protruding density and of the I27 structure, there is only one way to fit the NMR structure of I27 (PDB 1TIT (35)) that gives a good Fourier-shell correlation between the isolated I27 density and the map generated from the I27 PDB model (SI Appendix, Fig. S2). In the fitted model, the C-terminal end of I27 extends into the exit tunnel and a β-hairpin loop on ribosomal protein uL24 is lodged in a cavity in I27 (Figure 2B and Supporting Video S1). The I27 domain further packs against ribosomal protein uL29 and ribosomal 23S RNA (Figure 2C), as if it is being pulled tight against the ribosome by the nascent chain. We conclude that the peak at $L$ = 35-38 residues in the force profile indeed represents the cotranslational folding of the I27 domain at the tunnel exit.

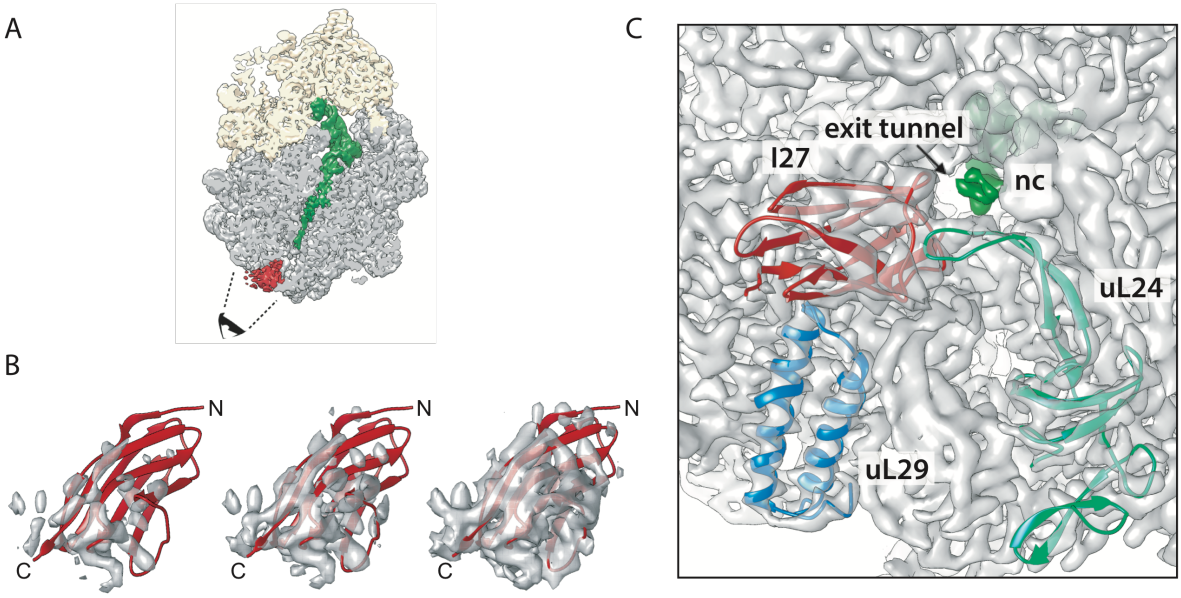


**Figure 2.** Cryo-EM structure of I27[$L$=35] RNCs. (A) Cryo-EM reconstruction of the I27–TnaC[$L$ = 35] RNC. The ribosomal small subunit is shown in yellow, the large subunit in grey, the peptidyl-tRNA with the nascent chain in green, and an additional density corresponding to I27 at the ribosome tunnel exit in red. The black cartoon eye and dash lines indicate the angle of view in panel (C). The density contour level for feature visualization is at 1.7 times root-mean-square deviation (1.7 RMSD). (B) Rigid-body fit of the I27 domain (PDB 1TIT) to the cryo-EM density map displaying from high (left) to low (right) contour levels at 2.6, 2.0 and 1.4 RMSD, respectively. N and C represent the N and C termini of the I27 domain, respectively. (C) View looking into the exit tunnel (arrow) with density for the nascent chain (nc) in dark green. Ribosomal proteins uL29 (blue; PDB 4UY8), uL24 (light green; the β hairpin close to I27 domain was re-modelled based on PDB 5NWY) and the

167 fitted I27 domain (red) are shown in cartoon mode; 23S RNA and proteins not contacting I27
168 are shown as density only. The density contour level is at 5 RMSD excluding tRNA, nascent
169 chain and I27 domain, which are displayed at 1.7 RMSD.

170

171 **Coarse-grained molecular dynamics simulations recapitulate I27 folding on the**
172 **ribosome**

173 The yield of folded protein in arrest peptide experiments has been used as a proxy for the
174 pulling forces that are exerted on the nascent chain at different points during translation in all
175 studies to date (1, 2, 29). Here, to further elucidate the molecular origins of these forces and
176 provide a quantitative interpretation of the observed folding yield of I27, we have calculated
177 force profiles based on coarse-grained MD simulations (see Methods). Briefly, in the MD
178 model, the 50S subunit of the *E. coli* ribosome (36) (PDB 3OFR) and the nascent chain are
179 explicitly represented using one bead at the position of the Cα atom per amino acid, and three
180 beads (for P, C4', N3) per RNA base (Figure 3A). The interactions within the protein were
181 given by a standard structure-based model (37-39), which allowed it to fold and unfold.
182 Interactions between the protein and ribosome beads were purely repulsive (40) and the
183 ribosome beads were fixed in space, as in previous simulation studies (18). I27 was
184 covalently attached to unstructured linkers having the same sequences as those used in the
185 force-profile experiments (Figure 3B) and the C terminus of the linker was tethered to the last
186 P atom in the A-site tRNA (41) with a harmonic potential, allowing the force exerted by the
187 folding protein to be directly measured. The potential chosen was stiff enough that
188 displacements caused by typical pulling forces were smaller than 1 Å. For each linker length
189 *L*, we used umbrella sampling to determine the average force exerted on the AP by the
190 protein in the folded and unfolded states while arrested, as well as the populations of those
191 two states (Figure 3C). We also estimated the folding and unfolding rates directly from
192 folding/unfolding simulations.

193

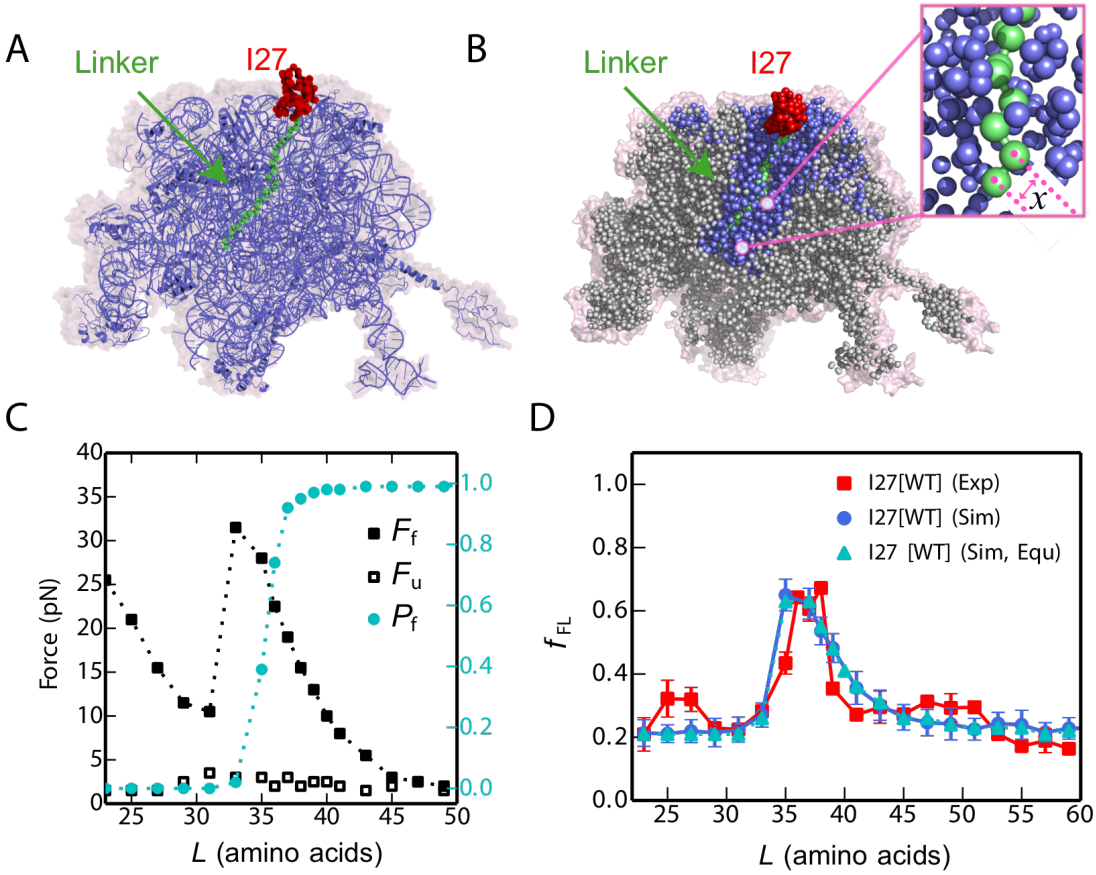


**Figure 3.** MD simulations of cotranslational folding of I27. (A) 50S subunit of the *E. coli* ribosome (PDB 3OFR) with I27[$L$=35] attached via an unstructured linker. (B) Coarse-grained model for I27 (red) and linker (green), with surrounding ribosomal pseudo-atoms in blue. Pseudo-atoms with grey colour are not used in the simulations. The instantaneous force exerted on the AP is calculated from the variation in the distance $x$ between the C-terminal Pro pseudo-atom and the next pseudo-atom in the linker (see inset). (C) Average forces exerted on the AP by the unfolded state ($F_u$, empty symbols) and folded state ($F_f$, filled symbols) of I27 at different linker lengths $L$. The average fraction folded I27 for different $L$, $P_f$, is shown in cyan on the right axis. Free energy profiles at each linker length are shown in SI Appendix, Fig. S4. (D) Experimental (red square) force profiles for cotranslational folding of I27. Force profiles calculated from simulations using full kinetic scheme or pre-equilibrium model are shown in blue circle and cyan triangle respectively. The RMSD of the $f_{FL}$ between experiment and simulation is 0.08.

Given the experimentally-determined force-dependence of the escape rate $k(F)$ (25), here approximated by a Bell-like model (42), we can calculate the expected escape rate while the protein is in the unfolded or folded state, from which the fraction full-length protein obtained with a given linker length and incubation time can be determined from a kinetic model, as described in Methods. The calculated $f_{FL}$ profile for I27 is shown in Figure 3D (see also SI

215 Appendix, Fig. S5) for the full solution of the kinetic model, as well as for an approximation
216 in which the folding and unfolding rates are assumed to be faster than the escape rate ("pre-
217 equilibrium"). Both results are very consistent with each other, as well as with the
218 experimental profile. The peak in the folding yield arises as consequence of two opposing
219 effects, the force exerted by the folding protein and population of the folded state, which
220 respectively decrease and increase as the linker length increases. In the simulations with the
221 I27[*L*=35] construct, the folded I27 domain is seen to occupy positions that largely overlap
222 with the cryo-EM structure (Supporting Video S2). Overall, these results suggest that the MD
223 model provides a good representation of the folding behaviour of the I27 domain in the
224 ribosome exit tunnel. To show that the simulation model is not specific to I27, we have also
225 applied it to another two proteins with different topologies for which experimental force
226 profiles have been recorded, Spectrin R16 (all-α fold) and S6 (α/β fold) (2, 29). In these
227 cases, we also obtain force profiles similar to experiment (SI Appendix, Fig. S6 and S7).

228

229 **Force profiles of I27 variants probe the folding pathway**

230 To test whether the cotranslational folding pathway is the same as that observed for the
231 isolated I27 domain *in vitro*, we investigated three destabilised variants of I27, both by
232 simulation and experiment. One mutation in the core, Leu 58 to Ala (L58A), located in β-
233 strand E (Figure 4A) destabilizes the protein by 3.2 kcal $mol^{-1}$, and removes interactions that
234 form early during folding of the isolated domain, playing a key role in formation of the
235 folding nucleus (ϕ-value = 0.8) (26). Two further mutations, M67A and deletion of the N-
236 terminal A-strand, remove interactions that form late in the folding of I27 (*i.e.*, both mutants
237 have low ϕ-values (26, 27)). The A-strand is the first part of I27 to emerge from the
238 ribosome, while M67 is located in a part of I27 that is shown by cryo-EM to be located in
239 very close proximity to a β hairpin loop of ribosomal protein uL24 in I27-TnaC[*L*=35] RNCs
240 (SI Appendix Fig. S3A). The interaction with the I27 domain shifts the tip of this uL24
241 hairpin by about 6 Å compared to its location in other RNC structures (SI Appendix Fig.
242 S3B).

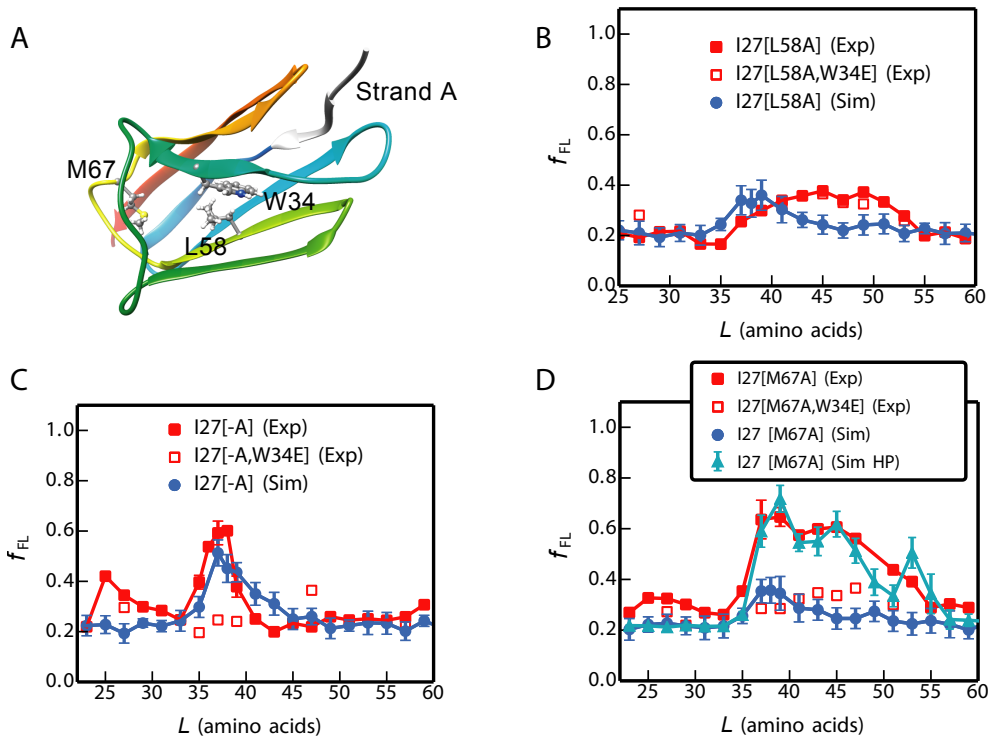


**Figure 4**. Simulations capture the experimental force profiles for mutant I27 domains. (A) Mutated residues in I27 (sticks). (B-D) Experimental (red) force profiles and calculated ones from full kinetic scheme (blue) for (B) I27[L58A], (C) A-strand deletion mutant I27[-A], (D) I27[M67A]. I27[M67A] (Sim HP) represents a simulation in which hydrophobic interactions between I27[M67A] and ribosome proteins uL23/uL29 are included. Experimental force profiles for non-folding mutants that contain an additional W34E mutation are shown as red open squares. The RMSD of the $f_{FL}$ between experiment and simulation for I27[L58A], I27[-A] are 0.07 and 0.08 respectively. For I27[M67A], the $f_{FL}$ RMSD is 0.07 between experiment and simulation (Sim HP).

The simulated force profile for the L58A variant predicts a much lower force peak than for wild-type I27; likewise, the experimental force peak is lower and broader than for wild-type, extending from $L$ = 37-53 residues (Figure 4B). The $f_{FL}$ values are very similar to those obtained for I27[L58A,W34E], a non-folding variant of I27[L58A]. Therefore, the weak forces seen at $L \approx$ 40-50 residues are not due to a folding event, indicating that I27[L58A] does not exert an appreciable force due to folding near the ribosome.

The A-strand comprises the first seven residues of I27 and removal of this strand, I27[-A], results in a destabilisation of 2.78 kcal mol$^{-1}$; however, both the simulated and experimental force profiles for I27[-A] are very similar to those for wild-type I27 (Figure 4C). Residue M67 is located in the E-F loop, and mutation to alanine results in a destabilisation of 2.75 kcal mol$^{-1}$; for this variant, folding commences at $L \approx$ 35 residues as for wild-type I27, but the peak is much broader (Figure 4D). Non-folding control experiments

266 for variants I27[-A,W34E], and I27[M67A,W34E] (Figure 4C and D) show that the peaks in
267 the force profiles for these variants are due to a folding event. These results show that
268 deletion of the A-strand and destabilisation of the E-F loop do not affect the onset of
269 cotranslational folding of I27, but that the M67A mutation increases the width of the folding
270 transition. The simulation model used for the other mutants does not predict such a broad
271 peak, suggesting that it may be necessary to include additional factors to reproduce the data
272 for M67A. One possibility which may explain the result would be favourable interactions of
273 the folded M67A mutant with the ribosome surface. The ribosomal surface proteins uL23 and
274 uL29 have been suggested to form a potential interaction site for nascent proteins such as
275 trigger factor (43), signal recognition particle (44) and SecYE (45). Here we have explored
276 the hypothesis that the broad force peak of mutant M67A might due to interactions between
277 an exposed hydrophobic cavity on I27[M67A] resulting from the mutation, and hydrophobic
278 surface residues of ribosomal proteins uL23 and uL29. By introducing such interactions into
279 the model, we are able to obtain a broad peak in the force profile very similar to that seen in
280 experiment (Figure 4D).

281 **The folding pathway is only subtly affected by the presence of the ribosome.**

282 To compare the folding pathways when the protein is folding near the tunnel exit or outside
283 the ribosome, we estimated ϕ-values based on the transition paths of I27 folding on the
284 ribosome from our coarse-grained simulations, using a method introduced previously(46).
285 The transition paths are those regions of the trajectory where the protein crosses the folding
286 barrier, here defined as crossing between $Q = 0.3$ and $Q = 0.7$. For each linker length, 30
287 transition paths were collected from MD simulations. To reduce the uncertainty in the
288 experimental reference data, we only compared with experimental ϕ-values if the change in
289 folding stability between the mutant and the wild type is sufficiently large ($|\Delta\Delta G| > 7$ kJ/mol)
290 (47). As seen in Figure 5A, when the linker is long ($L = 51$ residues) and I27 is allowed to
291 fold outside the ribosome, the calculated ϕ-values are consistent (Spearman correlation
292 $r$=0.80) with the experimental values obtained for the folding of isolated I27 *in vitro* (26). For
293 shorter linker lengths ($L = 31$ and 35 residues), calculated ϕ-values remain largely unchanged
294 except for a slight increase near the N terminus (around residues 3-6) and a slight decrease
295 near the C terminus (around residues 72-74) (Figure 5B and C).

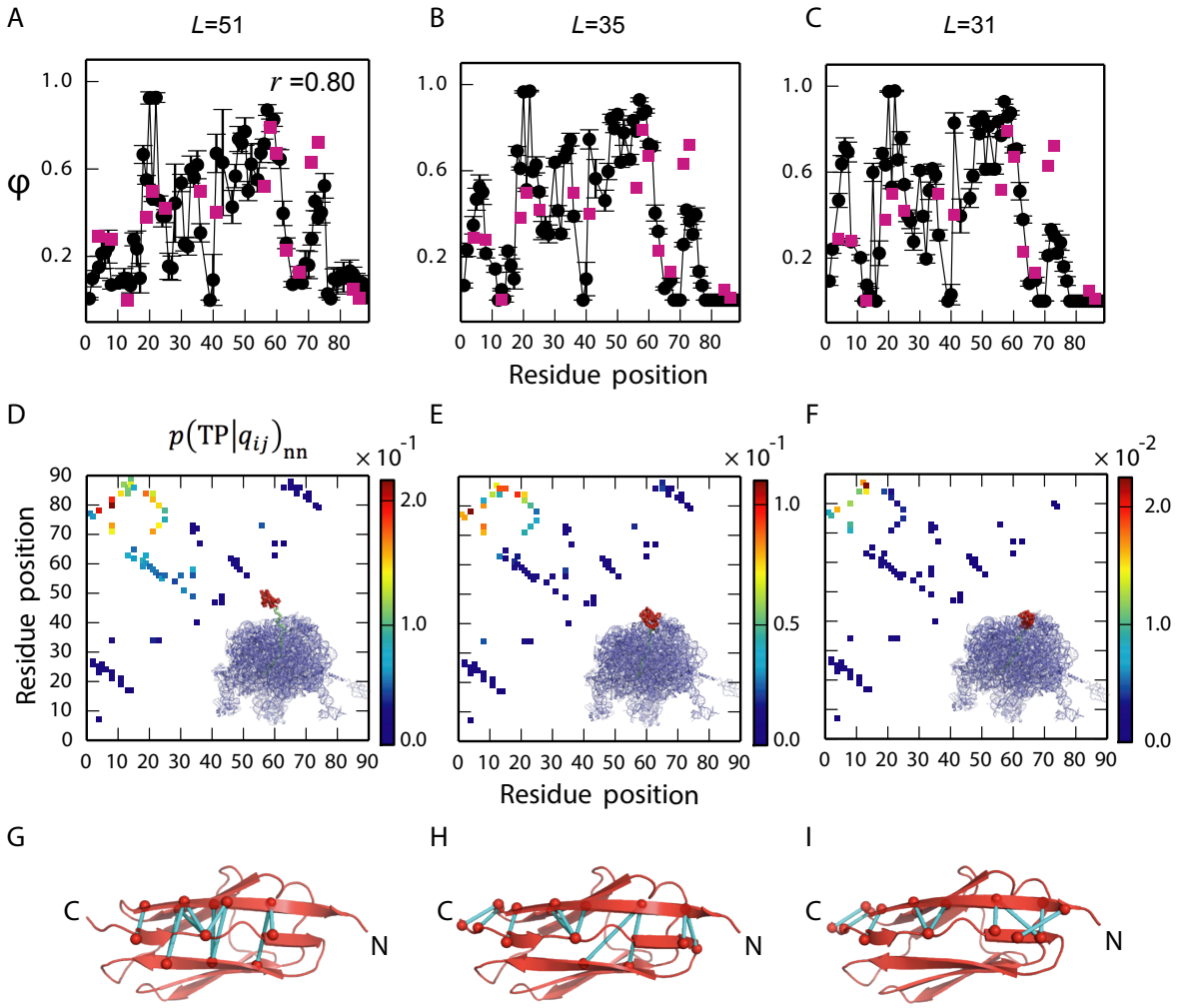


**Figure 5.** Simulated folding pathways for ribosome-tethered I27. LH column, $L$=51; middle column, $L$= 35; RH column, $L$=31. Top panels: Simulated ϕ-values for I27 (black). ϕ-values determined by *in vitro* folding of purified I27 are shown as red squares. At $L$=51 the simulated ϕ-values match well with experiment (spearman correlation $r$=0.80). At $L$=35 and $L$=31 the simulated ϕ-values are higher at the N terminus and lower at the C terminus, than the experimental values, reflecting a change in importance of these regions when I27 folds in the confines of the ribosome. Middle row: Relative probability that if a particular contact is formed then the protein is on a folding trajectory, $p(\mathrm{TP}|q_{ij})_{\mathrm{nn}}$. When the protein is constrained the limiting factor is formation of a few key contacts. A cartoon of the ribosome with I27 in red is shown on each panel. Bottom row: The top ten most important contacts are coloured in cyan on the native structure.

To obtain a more detailed picture regarding the relative importance of different native contacts in the folding mechanism, we computed the conditional probability of being on a transition path (TP), given the formation of a contact $q_{ij}$ between residues $i$ and $j$, $p(\mathrm{TP}|q_{ij})_{\mathrm{nn}}$ (48). This quantity indicates which native contacts are most important for

314 determining a successful folding event. $p(\mathrm{TP}|q_{ij})_{\mathrm{nn}}$ is closely related to the frequency of the
315 contact $q_{\mathrm{ij}}$ on transition paths $p(q_{ij}|\mathrm{TP})$, but is effectively normalized by the probability that
316 the contact is formed in non-native states $p(q_{ij})_{\mathrm{nn}}$, and can be expressed as:

317 $$p(\mathrm{TP}|q_{ij})_{\mathrm{nn}} = \frac{p(q_{ij}|\mathrm{TP})p(\mathrm{TP})_{\mathrm{nn}}}{p(q_{ij})_{\mathrm{nn}}} \quad [1]$$

318 where $p(\mathrm{TP})_{\mathrm{nn}}$ is the fraction of non-native states which are on transition paths at
319 equilibrium. The subscript nn means that only the non-native segments of a trajectory are
320 included, *i.e.*, unfolded states and transition paths; the native, folded state is not included in
321 the calculation since native contacts are always formed in this state. The simulations suggest
322 that formation of native contacts between the N and C termini is somewhat more important
323 when folding takes place in the mouth of the exit tunnel ($L$ = 31 residues) than far outside the
324 ribosome ($L$ = 51 residues) (Figure 5D-F, upper left-hand corner in the panels). This is likely
325 due to the greater difficulty of forming these contacts (examples are shown in Figure 5G-I)
326 under ribosomal confinement; therefore, forming them becomes more critical in enabling the
327 protein to fold.

328

329 **Discussion**

330 Using a combination of MD simulation, force-profile measurements and cryo-EM, we have
331 investigated the cotranslational folding pathway of the 89-residue titin I27 domain. I27 has
332 been extensively characterised in previous *in vitro* folding studies (26, 27, 49-60). Results
333 from all three techniques show that wild-type I27 folds in the mouth of the ribosome exit
334 tunnel; in the cryo-EM structure of I27-TnaC[$L$=35] RNCs, I27 packs against ribosomal
335 proteins uL24, uL29, and ribosomal 23S RNA. This is in apparent contrast to a previous
336 NMR study on another Ig-like protein, in which the domain was shown to acquire its native
337 fold (as reflected in the NMR spectrum) only when fully outside the ribosome tunnel, at $L$ =
338 42-47 residues linker length (20).

339 In order to determine the molecular origin of the measured force profile, we
340 performed molecular dynamics simulations of I27 folding on the ribosome, varying the
341 length of the linker sequence between the arrest peptide and the I27 domain. We calculated
342 the pulling force directly from the simulations and translated this into yield of folded protein
343 using a kinetic model parameterized based on known release kinetics of the SecM AP. This
344 enabled us to recapitulate the experimental arrest peptide force measurement profile, and

345 therefore relate $f_{FL}$ directly to the force exerted on the arrest peptide. Our simulations
346 demonstrate the direct effect that the restoring force of the nascent chain can have on
347 determining when the protein folds on the ribosome. We show that $f_{FL}$ depends upon a
348 combination of the force exerted by the folded protein and the fraction of folded protein at
349 the given linker length *L*.

350 In order to relate how destabilization of regions that fold early and late in the isolated
351 domain affects folding on the ribosome, we used simulations to predict the onset of folding in
352 three mutant variants of I27. A previous ϕ-value analysis of I27 (26) showed that early
353 packing of the structurally central β-strands drives the folding of this domain, while
354 peripheral strands and loop regions pack later in the folding process. Mutations in the folding
355 core (such as L58A) slow folding, whereas mutations in the periphery have no effect on
356 folding rates (26). L58 is a key residue in the critical folding nucleus and almost fully packed
357 in the transition state, in isolated domain studies. The simulated and experimental force
358 profiles of I27 [L58A] show that this variant does not fold in or near the exit tunnel; hence,
359 destabilisation of the central folding core prevents folding close to the ribosome. Since
360 isolated I27[L58A] is fully folded, it is likely that this variant can only fold cotranslationally
361 at longer linker lengths, when it is no longer in close proximity to the ribosome and exerts
362 little force on the nascent chain.

363 Our experiments show that I27 variants destabilized in regions of the protein that are
364 unstructured, or only partially structured, in the transition state, are still able to commence
365 folding close to the ribosome. The force profiles reveal that the onset of folding of mutants
366 with the A-strand deleted, or with the Met 67 to Ala mutation in the E-F loop, is the same as
367 for wild-type although these have a similar destabilisation as L58A (Figure 4). The broader
368 peak observed experimentally for M67A is harder to interpret. A plausible explanation is that
369 the mutation introduces non-specific interactions of the folded domain with the ribosome
370 surface, and we have shown that incorporating such interactions into the simulations could
371 reproduce the results. An additional factor may be that that the mutation is in a region that
372 interacts closely with ribosomal protein uL24 in the wild-type cryo-EM structure (SI
373 Appendix Fig. S3).

374 Our simulations reproduce the onset of folding in the three mutant variants of I27 (Figure 4),
375 and so give us the confidence to investigate how confinement within the ribosome affects the
376 folding pathway of I27. We used simulations to investigate the folding of I27 arrested on the
377 ribosome at various linker lengths, using a Bayesian method for testing the importance of

378 specific contacts on the folding pathway, as well as by computing ϕ-values (Figure 5).
379 Overall, we find that the mechanism and pathway of folding are robust towards variation in
380 linker length and relatively insensitive to the presence of the ribosome; small but significant
381 changes are observed only for contacts near the N and C termini. These shifts are consistent
382 with the greater importance of forming N-terminal contacts when the C terminus is
383 sequestered within the exit tunnel, possibly to compensate for loss of contacts at the C
384 terminus.

385 In our kinetic modelling, we found that we obtained similar results with or without the
386 assumption that folding and unfolding are fast relative to the escape rate, suggesting that this
387 "pre-equilibrium" assumption is justified, at least for this protein. The reason for its validity
388 in the case of I27 can be seen by comparing the folding and unfolding rates with the force-
389 dependent escape rate of ~ $2.4 \times 10^{-3}$ $s^{-1}$ obtained at the highest forces of ~20 pN (c.f., Fig.
390 3C). Folding and unfolding rates at different linker lengths can be obtained by combining the
391 linker-length dependence of the rates from simulation with the known folding/unfolding rates
392 for isolated I27 from experiment (SI Appendix, Fig. S9). The presence of the ribosome
393 increases the unfolding rate at shorter linker lengths so that it is faster than the maximum
394 escape rate, while not slowing the folding rate sufficiently for it to drop below the escape
395 rate. Note that the unfolding rate does drop below the maximum escape rate at larger linker
396 lengths, but by that point the folded population is already almost 100%, so the pre-
397 equilibrium assumption still gives accurate results. Although this assumption appears to be
398 justified in the case of I27, it is probably not true in general, and it will be interesting to
399 investigate for slower-folding proteins in future.

400 The arrest peptide experiments, in which a protein exerts a force due to folding in
401 some ways resemble atomic force microscopy or optical tweezer experiments in which an
402 external force is applied to the protein termini. It is important to note, however, that the
403 nature and effect of the forces exerted on the folding protein by tethering to the ribosome are
404 very different than is the case for pulling on both termini by an external force. For example,
405 forces of the magnitude seen in this work (up to ~20 pN) tend to have very little effect on the
406 unfolding rate when applied to the termini of I27, due to the similarity in extension of the
407 folded and transition states (61); by contrast folding rates are dramatically slowed, even by
408 very small forces, due to the large difference in extension of between unfolded and transition
409 states (56). The forces arising from tethering to the ribosome are due to the folding of the
410 protein itself rather than an external device. They arise from the constriction of available

411 configuration space, particularly for folded and partially folded states, as well as from any
412 attractive interactions between the protein and the ribosome. Our simulations suggest that for
413 I27, reducing the linker length speeds up unfolding and slows folding rates by similar factors.
414 Thus, it seems that comparisons to the effects of forces exerted by AFM and optical tweezer
415 experiments need to be performed with care.

416 We have previously shown that α-helical proteins can fold co-translationally (2),
417 perhaps unsurprising since helical structures are dominated by short-range interactions and
418 helices can form within the ribosome tunnel itself (62, 63). Here, our equilibrium arrest-
419 peptide assay and structural studies reveal that an all-β protein, titin I27, is able to fold within
420 the mouth of the ribosome exit tunnel, despite its folding being dominated by long-range
421 interactions. Molecular simulations, accounting for the effect of the entropic restoring force
422 on protein stability, reproduce the yield of protein from experiments remarkably well. These
423 simulations reveal that I27 folds on the ribosome by the same pathway as when the protein
424 folds away from the confines of the ribosome. We note that a similar conclusion has been
425 reached by Guinn et al. (64) for another small protein, src SH3, using a completely different
426 experimental approach which combines optical tweezer experiments and chemical denaturant
427 to characterize the folding pathway of src SH3. Thus, the evidence so far suggests that single-
428 domain proteins, both α-helical and β-sheet, can fold close to the ribosome. On the other
429 hand, while all-β proteins appear to fold by a similar pathway with or without the ribosome
430 present, there is evidence for α-helical proteins forming partially structured cotranslational
431 intermediates (11, 65) or folding by different pathways on the ribosome (2). This mechanistic
432 difference may relate partly to the small contact order of helical proteins, allowing partially
433 folded states to be more stable than for all-β proteins. The situation for multidomain proteins
434 is likely to be still more complicated, as some studies have already indicated (11, 23, 66, 67).

435

436 **Acknowledgements**

437 This work was supported by grants from the Knut and Alice Wallenberg Foundation, the
438 Swedish Cancer Foundation, and the Swedish Research Council to GvH, by grants from the
439 Deutsche Forschungsgemeinschaft (DFG) GRK 1721 and FOR1805 to RB, by a DFG
440 fellowship through the Graduate School of Quantitative Biosciences Munich (QBM) to TS,
441 and by the Wellcome Trust (WT095195) to JC; PT and RBB were supported by the
442 Intramural Research Program of the National Institute of Diabetes and Digestive and Kidney

443 Diseases of the National Institutes of Health; JC is a Wellcome Trust Senior Research
444 Fellow. The cryo-EM data were collected at the Swedish National Cryo-EM Facility funded
445 by the Knut and Alice Wallenberg Foundation, the Family Erling Persson Foundation and the
446 Science for Life Laboratory. This work utilized the computational resources of the NIH HPC
447 Biowulf cluster. (http://hpc.nih.gov)

448

449 **Materials and Methods**

450 **Enzymes and chemicals**

451 All enzymes were obtained from Thermo Scientific. Oligonucleotides were purchased from
452 Life Technologies. In-Fusion Cloning kits were obtained from Clontech and DNA
453 purification kits were purchased from Qiagen. PURExpress cell-free translation system was
454 obtained from Eurogentec. [35S]-methionine was purchased from Perkin Elmer. Instant Blue
455 protein stain was purchased from Expedeon.

456

457 **DNA manipulation**

458 Titin I27 constructs for *in vitro* translation were generated in pRSET A plasmid (Invitrogen)
459 (previously modified to remove the sequence including the entire T7 gene 10 leader and EK
460 recognition site up to, but not including, the *Bam*H I site and replaced with a sequence
461 encoding residues L, V, P, R, G, S) carrying the *E. coli* SecM arrest peptide
462 (FSTPVWISQAQGIRAGP) and a truncated *E. coli lepB* gene, under the control of a T7
463 promoter. Increasing linker lengths were generated in pRSET A by PCR; linear pRSET A
464 constructs (containing the SecM AP and truncated lepB, but lacking I27) were generated by
465 PCR using primers which extended the linker from 23 aa to 63 aa (in steps of 2 aa) from the
466 direction of the C to the N terminus. I27 flanked by GSGS linkers was amplified by PCR
467 with overhanging homology to the plasmid containing the desired linker length. Cloning was
468 performed using the In-Fusion system (Takara Bio USA, Inc.), according to the
469 manufacturer's instructions. The final two C-terminal residues (EL) of the 89 aa Titin I27
470 construct are not structured in the PDB file 1TIT, and are therefore included in the linker
471 region. The amino acid sequence of the construct I27[*L*=63] is as follows (I27 in bold and
472 SecM AP underlined):
473 MRGSHHHHHHGLVPRGSGS**LIEVEKPLYGVEVFVGETAHFEIELSEPDVHGQWK**
474 **LKGQPLAASPDCEIIEDGKKHILILHNCQLGMTGEVSFQAANTKSAANLKVK**EL

475 SGSGKFAYGIKDPIYQKTLVPGQQNATWIVPPGQYFMMGDWMSSFSTPVWISQAQG
476 IRAGPGSSDKQEGEWPTGLRLSRIGGIH**
477 The mutants I27[–A] (lacking β-strand A), I27[L58A] and I27[M67A] were generated for
478 each linker length by site-directed mutagenesis. For the wild-type I27 and I27[–A] constructs
479 with $L$ = 27, 35, 37, 39, 47 and 57 residues, site-directed mutagenesis was performed to
480 generate constructs with the non-functional FSTPVWISQAQGIRAGA arrest peptide
481 (mutated residue underlined) as full-length controls, and constructs with the crucial Pro, at
482 the end of the AP, substituted with a stop codon as arrest controls. Site-directed mutagenesis
483 was performed to generate W34E variants as non-folding (nf) controls at $L$ = 27, 29, 31, 35,
484 37, 39, 41, 43, 47, 49, 51 and 57 for wild-type I27; $L$ = 27, 35, 37, 39, 47 and 57 residues for
485 I27[–A]; $L$ = 27, 41, 45, 47, 49 and 53 residues for I27[L58A]; $L$ = 27, 29, 37, 39, 41, 43, 45,
486 47 and 51 residues for I27[M67A]. All constructs were verified by DNA sequencing.

487 **In vitro transcription and translation**

488 Transcription and translation were performed using the commercially available PURExfrex *in*
489 *vitro* system (GeneFrontier Corporation), according to the manufacturer's protocol, using 250
490 μg plasmid DNA as template. Synthesis of [$^{35}$S]-Met-labeled polypeptides was performed at
491 37 °C, 500 r.p.m. for exactly 15 min. The reaction was quenched by the addition of an equal
492 volume of 10% ice-cold trichloroacetic acid (TCA). The samples were incubated on ice for
493 30 min and centrifuged for 5 min at 20,800 × $g$ and 4 °C. Pellets were dissolved in sample
494 buffer and treated with RNase A (400 μg ml$^{-1}$) for 15 min at 37 °C before the samples were
495 resolved by SDS-PAGE and imaged on a Typhoon Trio or Typhoon 9000 phosphorimager
496 (GE Healthcare). Bands were quantified using ImageJ to obtain an intensity cross section,
497 (http://rsb.info.nih.gov/ij/), which was subsequently fit to a Gaussian distribution using in-
498 house software (Kaleidagraph, Synergy Software). The fraction full-length protein, $f_{FL}$, was
499 calculated as $f_{FL} = I_{FL}/(I_{FL}+I_A)$, where $I_{FL}$ and $I_A$ are the intensities of the bands representing
500 the full-length and arrested forms of the protein. For wild-type I27 and six nf control samples
501 ($L$ = 27, 35, 37, 39, 47 and 57 residues), *in vitro* transcription and translation were also
502 performed at 37 °C, 500 r.p.m. for exactly 30 min. The resultant force profile was slightly
503 higher than that obtained at 15 min but has essentially the same shape (SI Fig. S5).

504 The reproducibility of force profile data has been discussed previously (2). For wild-type I27,
505 data points $L$ = 61 and 63 residues are a single experiment; $L$ = 33, 36, 38, 45, 53, 55 and 59
506 residues are an average of 2 experiments; all other values of $L$ are an average of at least 3
507 experiments. For I27[–A] strand, $L$ = 23, 25, 33, 41, 43, 51, 53, 55 residues are a single

508 experiment; all other values of *L* are an average of 2 experiments, except *L* = 35, 37 and 39
509 residues which are an average of at least 3 experiments. For I27[L58A], all data points are a
510 single experiment except *L* = 27, 37, 41, 45, 47, 49 and 53 residues, which are an average of
511 2 experiments. For I27[M67A], *L* = 23, 25 and 51 – 63 residues are a single experiment; *L* =
512 29 – 35 residues are an average of 2 experiments; *L* = 27, 37 – 47 and 51 residues are an
513 average of at least 3 experiments. For wild-type I27 samples incubated for 30 min, all data
514 points are a single experiment except *L* = 27, 35, 37, 39, 47 and 57 residues, which are an
515 average of 2 experiments. For non-folding controls, all data points are a single experiment
516 except for wild-type I27 *L* = 29, 31, 39, 43 and 47 residues which are an average of 2
517 experiments.

518 **Cloning and purification of ribosome-nascent chain complexes**

519 The I27 construct at *L* = 35, which is at the peak of $f_{FL}$ (Figure 1B), was studied by cryo-EM.
520 The SecM AP in these constructs was substituted with the TnaC AP (34) for more stable
521 arrest, and the constructs were engineered to maintain a linker length of 35 amino acid
522 residues. An N-terminal 8X His tag was introduced to enable purification. The amino acid
523 sequence of the construct used was (I27 in bold and TnaC AP underlined):

524 MDMGHHHHHHHHDYDIPTTLEVLFQGPGT**LIEVEKPLYGVEVFVGETAHFEIELS**
525 **EPDVHGQWKLKGQPLAASPDCEIIEDGKKHILILHNCQLGMTGEVSFQAANTKS**
526 **AANLKVK**ELSGSGSGSGGPNILHISVTSKWFNIDNKIVDHRP**

527 The construct was engineered into a pBAD expression vector, under the control of an
528 arabinose-inducible promoter. The translation-initiation region was optimized as described in
529 (68). The plasmid was transformed into the *E. coli* KC6 *ΔsmpB ΔssrA* strain. 4 colonies were
530 picked and tested for expression of the RNCs at 37°C in Lysogeny broth (LB).

531 Large-scale purification of RNCs was carried out based on a protocol described in (34).
532 Briefly, a single colony of the KC6 cells found to express the RNCs was picked and cultured
533 in LB at 37°C to an $A_{600}$ of 0.5. Expression was induced with 0.3% arabinose and was carried
534 out for 1 hour. Thereafter, the cells were chilled on ice, harvested by centrifugation, and
535 resuspended in Buffer A at pH 7.5 (50 mM HEPES-KOH, 250 mM KOAc, 2 mM
536 Tryptophan, 0.1% DDM, 0.1% Complete protease inhibitor). Cell lysis was carried out by
537 passing the cell suspension thrice through the Emulsifex (Avestin) at 8000 psi at 4°C. The
538 lysate was cleared of cell debris by centrifugation at 30,000xg for 30 min in the JA25-50
539 rotor (Beckman Coulter). The supernatant obtained was loaded on a 750 mM sucrose cushion

540 (in Buffer A) and centrifuged at 45, 000 x g for 24 hours in a Ti70 rotor (Beckman Coulter)
541 to obtain a crude ribosomal pellet, which was resuspended in 200 µl Buffer A by shaking
542 gently on ice.

543 RNCs from the crude suspension were purified via their His tags by affinity purification
544 using Talon (Clontech) beads, which was pre-incubated with 10 µg/ml tRNA to reduce
545 unspecific binding of ribosomes. The suspension was incubated with the beads for 1 hour at
546 4°C and subsequently washed with 20 column volumes of Buffer B at pH 7.5 (50 mM
547 HEPES-KOH, 10 mM $Mg(OAc)_2$, 0.1% Complete Protease Inhibitor, 250 mM sucrose, 2
548 mM Tryptophan). RNCs were eluted by incubating the Talon beads with Buffer C at pH 7.5
549 (50 mM HEPES, 150 mM KOAc, 10 mM $Mg(OAc)_2$, 0.1% Complete protease inhibitor, 150
550 mM imidazole, 250 mM sucrose) for 15 minutes and subsequently collecting the flow-
551 through. Elution was carried out thrice and the eluents were concentrated by centrifugation at
552 40,000 rpm for 2.5 hours in a TLA 100.3 rotor (Beckman Coulter). The pellet obtained at the
553 end of this step was gently suspended in a minimal volume of Buffer D at pH 7 (20 mM
554 HEPES-KOH, 50 mM KOAc, 5 mM $Mg(OAc)_2$, 125 mM sucrose, 2 mM Trp, 0.03% DDM).

555 **Cryo-EM sample preparation, data collection, processing and accession codes**

556 Approximately 4 $A_{260}$/ml units of RNCs were loaded on Quantifoil R2/2 grids coated with
557 carbon (3 nm thick) and vitrified using the Vitrobot Mark IV (FEI-Thermo) following the
558 manufacturer's instructions. Cryo-EM data was collected at the Cryo-EM National Facility at
559 the Science for Life Laboratory in Stockholm, Sweden.

560 Data was acquired on a 300 keV Titan Krios microscope (FEI) equipped with a K2 camera
561 and a direct electron detector (both from Gatan). The camera was calibrated to achieve a
562 pixel size of 1.06 Å at the specimen level. 30 frames were acquired with an electron dose
563 0.926 $e^-/Å^2$/frame and a total dose of 27.767 $e^-/Å^2$ and defocus values between -1 to -3 µm.
564 The first two frames were discarded and the rest were aligned using MotionCor2 (69). Raw
565 images were cropped into squares by RELION 2.1 beta 1 (70). Power-spectra, defocus values
566 and estimation of resolution were determined using the Gctf software (71) and all 2,613
567 micrographs were manually inspected in real space, in which 2,613 were retained. 468,015
568 particles were automatically picked by Gautomatch (http://www.mrc-lmb.cam.ac.uk/kzhang/)
569 using the *E. coli* 70S ribosome as a template. Single particles were processed by RELION 2.1
570 beta 1 (70). After 80 rounds of 2D classification, 384,039 particles were subjected to 3D
571 refinement using the *E. coli* 70S ribosome as reference structure, followed by 160 rounds of

572 3D classification without masking and 25 rounds of tRNA-focused sorting. One major class
573 containing 301,510 particles (64% of the total) was further refined including using a 50S
574 mask, resulting in a final reconstruction with an average resolution of 3.2 Å (0.143 FSC). The
575 local resolution was calculated by ResMap (72). Finally, the final map was obtained by local
576 B-factoring followed by low-pass filtering to 4.5 Å by RELION 2.1 beta 1 (70) in order to
577 best demonstrate the I27 domain.

578 For interpretation of the cryo-EM density, the cryo-EM structure model (PDB 4YU8) of *E.*
579 *coli* TnaC-stalled ribosome was fitted into corresponding density using UCSF Chimera (73).
580 The NMR model (PDB 1TIT) of I27 domain was fitted into the extra density of TnaC-stalled
581 ribosome using UCSF Chimera (73). Since the I27 domain represents a flat ellipsoid, we used
582 all four major and minor axes covering all possible orientations of the model fitting within
583 the density to validate the orientation of the fitted I27 model. Briefly, the model with four
584 different orientations were converted into densities (8 Å) by UCSF Chimera, and the cross-
585 correlation coefficients of each model map and the isolated I27 density were calculated by
586 RELION 2.1 beta 1 (70). Finally, uL24 β hairpin was remodeled as the tip of the hairpin is
587 shifted due to the existence of I27 domain.

588 Figures showing electron densities and atomic models were generated using UCSF Chimera
589 (73). Electron densities are shown at multiple contour levels in Figure 2 and SI Appendix, Fig.
590 S1. The contour levels relative to the root-mean-square deviation (RMSD) were calculated
591 from the final map values. Final map contains the volume for the entire RNC including the
592 I27 domain.

593 Coordinates for the cryo-EM map of the ribosome with the I27 domain density have been
594 deposited at the EMDataBank under accession code EMD-*xxxx*. Coordinates of fitted *E.coli*
595 TnaC-stalled ribosome (PDB 4UY8; uL24 remodeled) and I27 domain (PDB 1TIT) models
596 for interpreting the cryo-EM map have been deposited at the ProteinDataBank under
597 accession code *xxxx*.

598 **Coarse-grained molecular simulations**

599 The 50S subunit of the *E. coli* ribosome (PDB 3OFR (36)) and the nascent chain are
600 explicitly represented using one bead at the position of the α-carbon atom of each amino
601 acid, and three beads (for P, C4', N3) per RNA residue (Figure 2A). The interactions within
602 the protein were given by a standard structure-based model (37-39), which allowed it to fold

603 and unfold. Interactions between the protein and ribosome beads were purely repulsive (40)
604 and given by the same form of potential as for the structure-based model(37-39),

605 $$V_{ij} = \varepsilon_{ij}\left[\frac{A}{{r_{ij}}^{12}} - \frac{B}{{r_{ij}}^{10}} + \frac{C}{{r_{ij}}^{6}}\right] \quad [2]$$

606 where $r_{ij}$ is the distance between two beads $i$ and $j$, $\varepsilon_{ij}$ (=0.001 kJ/mol) sets the strength of
607 the repulsive interactions. The amino acid, phosphate, sugar and base are assigned radii $\sigma_i =$
608 4.5, 3.2, 5.1 and 4.5 Å respectively, and coefficients in Eq. 2 for interactions between protein
609 and ribosome beads $i$,$j$ are obtained from the mixing rules A = $\sqrt{{\sigma_i}^{12}{\sigma_j}^{12}}$ , B = $\frac{2}{{\sigma_i}^{-10}+{\sigma_j}^{-10}}$
610 and C = $\sqrt{{\sigma_i}^{6}{\sigma_j}^{6}}$.

611 During the simulations, the positions of the ribosome atoms were fixed in space, as in
612 previous studies (18). The linker between the AP and I27 was tethered by its C terminus to
613 the last P atom of the A-site tRNA, but was otherwise free to fluctuate. The trajectory was
614 propagated via Langevin dynamics, with a friction coefficient of 0.1 $ps^{-1}$ and a time step of
615 10 fs, at 291 K in a version of the Gromacs 4.0.5 simulation code, modified to implement the
616 potential given by Eq. 2 (74). All bonds (except the one used to measure force, below) were
617 constrained to their equilibrium length using the LINCS algorithm (75). The attractive
618 interactions between I27[M67A] and the hydrophobic residues (A, V, L, I, F, M, Y, W) on
619 the surface of uL23 and uL29 are modelled as (76):

620 $$V_{ij} = 4\varepsilon\left[\left(\frac{\sigma}{r_{ij}}\right)^{12} - \left(\frac{\sigma}{r_{ij}}\right)^{6}\right], \quad [3]$$

621 where $r_{ij}$ is the distance between residues $i$ and $j$, $\sigma$ is the range of the interaction and $\varepsilon$
622 represent the strength of the interaction. $\sigma$ and $\varepsilon$ are fixed at 6 Å and 5 kJ/mol respectively.
623 Residues of I27[M67A] which are involved in the attractive interactions are defined as the
624 ones whose heavy atoms are within 4.5 Å of any heavy atoms from residue 67 in the native
625 state.

626 To calculate the pulling force exerted on the nascent chain by the folding of I27, the bond
627 between the last and the second last amino acid of the SecM AP was modelled by a harmonic
628 potential as a function the distance between these two atoms, $x$ (Figure 3B):

629 $$E = \frac{1}{2}k_s(x - x_0)^2 \quad [4]$$

630 where $x_0$ is a reference distance. Here $x_0$ is set to 3.8 Å, which is the approximate distance
631 between adjacent Cα atoms in protein structures and $k_s$ is a spring constant, set to 3000
632 kJ.mol$^{-1}$.nm$^{-2}$. The value of $k_s$ was chosen so that the average displacement $x - x_0$ remains
633 below 1 Å for forces up to ~500 pN, which is much larger than the forces actually exerted by
634 the folding protein. The pulling force on the nascent chain was measured by the extension of
635 this bond as $F = -k_s(x - x_0)$.

636 I27 was covalently attached to unstructured linkers having the same sequences as used in the
637 force-profile experiments (see Figure 2B). Linker amino acids are repulsive to both the
638 ribosome and I27 beads, with interaction energy as described in Eq. 2.

639 The protein in its arrested state is subject to force $F(t)$, which will fluctuate, for example
640 when the protein folds or unfolds. The rate of escape from arrest has been shown to be force-
641 dependent (25); here we approximate the sensitivity to force using the phenomenological
642 expression originally proposed by Bell (42)

643 $$k(F) = k_0 e^{\beta F \Delta x^{\ddagger}}, \quad [5]$$

644 where $k_0$ is a zero-force rupture rate, $\Delta x^{\ddagger}$ is the distance from the free energy minimum to
645 the transition state, $\beta = 1/k_B T$ where $k_B$ is Boltzmann's constant and $T$ the absolute
646 temperature. While there are functions to describe force-dependent rates with stronger
647 theoretical basis, we use the Bell equation due to its simplicity and because its parameters
648 have previously been estimated from optical tweezer experiments for the SecM AP. In all
649 cases, we set $k_0$ (Eq. 5) to 3.4 ×10$^{-4}$ s$^{-1}$ and $\Delta x^{\ddagger}$ to 3.2 Å, based on the values determined by
650 Goldman *et al.* (they estimated $k_0$ and $\Delta x^{\ddagger}$ to be in the range of 0.5 ×10$^{-4}$ to 20 ×10$^{-4}$ s$^{-1}$ and
651 1-8 Å, respectively) (25).

652 We assume the probability of remaining on the ribosome $S(t) = 1 - f_{FL}(t)$ assuming that
653 $\dot{S} = -k(F(t))$, hence

654 $$S(t) = \exp[-\int_0^t k(F(t))dt]. \quad [6]$$

655 The escape of I27 from the ribosome can be described using kinetic model shown in SI
656 Appendix, Fig. S8 which explicitly takes into account the linker length-dependent
657 folding/unfolding rates of the I27 nascent chain, $k_u(L)$ and $k_f(L)$, on the ribosome, and the
658 force-dependent rate of escape from ribosome: $k(F_u(L))$ and $k(F_f(L))$. To estimate $k_f$ at
659 different linker lengths, we first carried out unbiased MD simulations to estimate the mean

first passage time for folding $t_{\mathrm{F}}^{\mathrm{mfpt}}$, from which the folding rate can be calculated as $k_{\mathrm{f}}^{\mathrm{wt}} = 1/\, t_{\mathrm{F}}^{\mathrm{mfpt}}$. Similarly, the unfolding rate can be calculated from unfolding simulations as $k_{\mathrm{u}}^{\mathrm{wt}} = 1/\, t_{\mathrm{u}}^{\mathrm{mfpt}}$. Since the rates in coarse-grained simulations are naturally much faster than in experiment, we globally scale the unfolding rates $k_{\mathrm{u}}^{\mathrm{wt}}$($L$=21, 23 …61) at different linker lengths so that $k_{\mathrm{u}}^{\mathrm{wt}}$ at very long linker lengths ($L$=61) is equal to the unfolding rate of isolated I27 ($4.9\times10^{-4}$ $s^{-1}$). Similarly, $k_{\mathrm{f}}^{\mathrm{wt}}$($L$=21, 23 …61) is scaled so that the $k_{\mathrm{f}}^{\mathrm{wt}}$ of I27 RNC[L=61] is equal to the unfolding rate of isolated I27 (SI Appendix, Fig. S9). For consistency with our pre-equilibrium solution, we further scale $k_{\mathrm{f}}^{\mathrm{wt}}$ to match the stability of I27 RNC[L=61] in our simulation model, yielding $k_{\mathrm{u}}^{\mathrm{wt}}$ and $k_{\mathrm{f}}^{\mathrm{wt}}$ at L=61 of $4.9\times10^{-4}$ $s^{-1}$ and 0.14 $s^{-1}$ (SI Appendix, Fig. S9) respectively. The same scaling method has been applied to the folding and unfolding rates of all mutants (I27[L58A], I27[M67A] and I27 [-A]) so that the folding/unfolding rates of the mutant RNC are consistent with the relative experimental values measured for the isolated mutants(26).

With the rates obtained from above, the time dependent survival probability $S(t)$ is estimated by the kinetic Monte Carlo method (the Bortz-Kalos-Lebowitz algorithm (77)). The system is initialized at the state when the unfolded nascent chain just emerges from the ribosome tunnel (UA, SI Appendix, Fig. S8) at time t=0. At each Monte Carlo step, a uniform random number $\delta$ between 0 and 1 is chosen, and a transition from the current state state $s$ to state $j$ will occur for the state $j$ which satisfies $\sum_{i=1}^{j-1} k_{si} < \delta \sum_{i=1}^{N} k_{si} < \sum_{i=1}^{j} k_{si}$, where $k_{si}$ represents the transition rate from state $s$ to state $i$. The time is updated by $t = t + \Delta t$, where $\Delta t = -(\delta')/\sum_{i=1}^{N} k_{si}$. $\delta'$ is a new number randomly chosen between 0 to 1.

The solution to the kinetic model can be simplified if we further assume that the escape from the ribosome is slow relative to the folding and unfolding of the protein. In this situation, we can approximate $S(t)$ in terms of the mean forces experienced when the protein is unfolded, $F_{\mathrm{u}}$, or folded, $F_{\mathrm{f}}$, and the unfolded and folded populations of $P_{\mathrm{u}}$ and $P_{\mathrm{f}}$ respectively,

$$S(t) \approx \exp\left[-t\left[P_{\mathrm{u}}k(F_{\mathrm{u}}) + P_{\mathrm{f}}k(F_{\mathrm{f}})\right]\right]. \quad [7]$$

The equilibrium properties of the system for each linker length were obtained from umbrella sampling using the fraction of native contacts $Q$ as the reaction coordinate, allowing $P_{\mathrm{u}}$, $P_{\mathrm{f}}$

690 and $F_u$, $F_f$ to be determined (Figure 3C). The details of the definition of $Q$ have been
691 previously described (48); in short, $Q$ is defined as

692 $$Q = \frac{1}{N}\sum_{(i,j)} \frac{1}{1 + e^{(r_{ij} - \lambda r_{ij}^0)}}, \quad [8]$$

693 where the sum runs over the N pairs of native contacts $(i, j)$, $r_{ij}$ is the distance between $i$ and
694 $j$ in configuration, $r_{ij}^0$ is the distance between $i$ and $j$ in the native state, λ =1.2 which
695 accounts for fluctuations when the contact is formed. A boundary of $Q$ = 0.5 is used to
696 separate folded from unfolded states.

697 In order to characterize folding mechanism, we used transition paths from folding
698 simulations for the $L$ = 51 case at 291 K. 50 independent simulations, each started from fully
699 extended configurations, were carried out for 4 microseconds. The folding barriers for the $L$ =
700 31 and 35 cases are very high at the same temperature, therefore the transition paths are
701 obtained from unfolding simulations instead. Starting from native-like folded
702 configurations, 50 unfolding simulations were carried out, with each trajectory being 4
703 microseconds long. Transition paths were defined as those portions of the simulation
704 trajectory from the last time I27 samples the configuration with $Q$ < 0.3 till the first time it
705 samples a configuration with Q > 0.7 (in the folding direction; opposite for unfolding). ϕ-
706 Values were computed from the transition paths using the approximation:

707 $$\phi(i) \approx \sum_{j:(i,j)\in\text{native}} p(q_{ij}|TP)$$

708 In which $p(q_{ij}|TP)$ is the probability that the native contact $q_{ij}$ between residues $i$ and $j$ is
709 formed on transition paths as defined above. We also characterized the importance of
710 individual contacts in determining the folding mechanism using $p(\text{TP}|q_{ij})_{\text{nn}}$, defined in Eq.
711 1 of the main text, i.e. the probability of being on a transition path given that contact $q_{ij}$ is
712 formed and the protein is not yet folded. Having already calculated $p(q_{ij}|TP)$ above,
713 evaluating $p(TP|q_{ij})_{\text{nn}}$ required $p(q_{ij})_{\text{nn}}$, the probability of a contact being formed in all
714 non-native fragments of the trajectory, and $p(\text{TP})$, the fraction of time spent on transition
715 paths. For $L$=51, we obtained $p(q_{ij})_{\text{nn}}$ directly from unbiased folding simulations, using the
716 portion of the trajectory up to the first folding event (i.e. the first time $Q$ > 0.7). For $L$=31 or

35, where the protein is still relatively unstable, we determined it from unfolding simulations by computing $p(q_{ij})$ separately for the unfolded and transition-path portions of the trajectory and combining them weighted by $p(\mathrm{TP})_{\mathrm{nn}}$. We determined $p(\mathrm{TP})_{\mathrm{nn}}$ via folding ($L$ = 51 case) and unfolding ($L$ = 31 and $L$ = 35 cases) simulations (described above). For the $L$ = 51 case, $p(\mathrm{TP})_{\mathrm{nn}} = \frac{2t_{\mathrm{TP}}}{2t_{\mathrm{TP}}+t_{\mathrm{F}}^{\mathrm{mfpt}}}$, where $t_{\mathrm{TP}}$ is the mean transition path time and $t_{\mathrm{F}}^{\mathrm{mfpt}}$ is the mean first passage time for folding obtained from the maximum likelihood estimator $t_{\mathrm{F}}^{\mathrm{mfpt}} = [N_{\mathrm{fold}}t_{\mathrm{fold}} + (N - N_{\mathrm{fold}})t_{\mathrm{sim}}]/N_{\mathrm{fold}}$, where $N$ is the total number of trajectories ($N = 50$), $N_{\mathrm{fold}}$ is the number of trajectories folding within 4 μs, $t_{\mathrm{fold}}$ is the average folding time (of the trajectories which fold), and $t_{\mathrm{sim}}$ is the length of the simulations (4 μs). For the $L$ = 31 and $L$ = 35 cases, it is less efficient to obtain the folding time $t_{\mathrm{F}}^{\mathrm{mfpt}}$ directly, therefore we estimate it based on the mean first passage time for unfolding, $t_{\mathrm{U}}^{\mathrm{mfpt}}$, from unfolding simulations. $p(\mathrm{TP})_{\mathrm{nn}} = \frac{2t_{\mathrm{TP}}}{2t_{\mathrm{TP}}+\frac{p_U}{p_F}t_{\mathrm{U}}^{\mathrm{mfpt}}}$, where $p_U$ and $p_F$ are the equilibrium populations of the unfolded and folded respectively determined from umbrella sampling.

## References


1. Nilsson OB, Hedman R, Marino J, Wickles S, Bischoff L, Johansson M, Muller-Lucks A, Trovato F, Puglisi JD, O'Brien EP, Beckmann R, & von Heijne G (2015) Cotranslational Protein Folding inside the Ribosome Exit Tunnel. *Cell Rep* 12(10):1533-1540.
2. Nilsson OB, Nickson AA, Hollins JJ, Wickles S, Steward A, Beckmann R, von Heijne G, & Clarke J (2017) Cotranslational folding of spectrin domains via partially structured states. *Nat Struct Mol Biol* 24(3):221-225.
3. Nilsson OB, Muller-Lucks A, Kramer G, Bukau B, & von Heijne G (2016) Trigger Factor Reduces the Force Exerted on the Nascent Chain by a Cotranslationally Folding Protein. *J Mol Biol* 428(6):1356-1364.
4. Anfinsen CB (1973) Principles that govern the folding of protein chains. *Science* 181(4096):223-230.
5. Onuchic JN, Luthey-Schulten Z, & Wolynes PG (1997) Theory of protein folding: the energy landscape perspective. *Annu Rev Phys Chem* 48(1):545-600.
6. Dill KA & Chan HS (1997) From Levinthal to pathways to funnels. *Nat Struct Biol* 4(1):10-19.
7. Tycko R (2004) Progress towards a molecular-level structural understanding of amyloid fibrils. *Curr Opin Struct Biol* 14(1):96-103.
8. Clark PL (2004) Protein folding in the cell: reshaping the folding funnel. *Trends Biochem Sci* 29(10):527-534.
9. Dobson CM (2001) Protein folding and its links with human disease. *Biochem Soc Symp* (68):1-26.

754 10. Gloge F, Becker AH, Kramer G, & Bukau B (2014) Co-translational mechanisms of
755 protein maturation. *Curr Opin Struct Biol* 24:24-33.
756 11. Holtkamp W, Kokic G, Jager M, Mittelstaet J, Komar AA, & Rodnina MV (2015)
757 Cotranslational protein folding on the ribosome monitored in real time. *Science*
758 350(6264):1104-1107.
759 12. Thommen M, Holtkamp W, & Rodnina MV (2017) Co-translational protein folding:
760 progress and methods. *Curr Opin Struct Biol* 42:83-89.
761 13. Krobath H, Shakhnovich EI, & Faísca PF (2013) Structural and energetic
762 determinants of co-translational folding. *J Chem Phys* 138(21):215101.
763 14. Tanaka T, Hori N, & Takada S (2015) How co-translational folding of multi-domain
764 protein is affected by elongation schedule: molecular simulations. *PLOS Comput Biol*
765 11(7):e1004356.
766 15. Wruck F, Katranidis A, Nierhaus KH, Buldt G, & Hegner M (2017) Translation and
767 folding of single proteins in real time. *Proc Natl Acad Sci U S A* 114(22):E4399-
768 E4407.
769 16. Jacobs WM & Shakhnovich EI (2017) Evidence of evolutionary selection for
770 cotranslational folding. *Proc Natl Acad Sci U S A* 114(43):11434-11439.
771 17. Samelson AJ, Jensen MK, Soto RA, Cate JH, & Marqusee S (2016) Quantitative
772 determination of ribosome nascent chain stability. *Proc Natl Acad Sci U S A*
773 113(47):13402-13407.
774 18. O'Brien EP, Christodoulou J, Vendruscolo M, & Dobson CM (2011) New scenarios
775 of protein folding can occur on the ribosome. *J Am Chem Soc* 133(3):513-526.
776 19. Knight AM, Culviner PH, Kurt-Yilmaz N, Zou T, Ozkan SB, & Cavagnero S (2013)
777 Electrostatic effect of the ribosomal surface on nascent polypeptide dynamics. *ACS*
778 *Chem Biol* 8(6):1195-1204.
779 20. Cabrita LD, Cassaignau AME, Launay HMM, Waudby CA, Wlodarski T, Camilloni
780 C, Karyadi ME, Robertson AL, Wang X, Wentink AS, Goodsell L, Woolhead CA,
781 Vendruscolo M, Dobson CM, & Christodoulou J (2016) A structural ensemble of a
782 ribosome-nascent chain complex during cotranslational protein folding. *Nat Struct*
783 *Mol Biol* 23(4):278-285.
784 21. Fedorov AN & Baldwin TO (1995) Contribution of cotranslational folding to the rate
785 of formation of native protein structure. *Proc Natl Acad Sci U S A* 92(4):1227-1231.
786 22. Nicola AV, Chen W, & Helenius A (1999) Co-translational folding of an alphavirus
787 capsid protein in the cytosol of living cells. *Nat Cell Biol* 1(6):341-345.
788 23. Ugrinov KG & Clark PL (2010) Cotranslational folding increases GFP folding yield.
789 *Biophys J* 98(7):1312-1320.
790 24. Evans MS, Clarke TF, & Clark PL (2005) Conformations of co-translational folding
791 intermediates. *Protein Pept Lett* 12(2):189-195.
792 25. Goldman DH, Kaiser CM, Milin A, Righini M, Tinoco I, Jr., & Bustamante C (2015)
793 Mechanical force releases nascent chain-mediated ribosome arrest *in vitro* and *in vivo*.
794 *Science* 348(6233):457-460.
795 26. Fowler SB & Clarke J (2001) Mapping the folding pathway of an immunoglobulin
796 domain: structural detail from Phi value analysis and movement of the transition state.
797 *Structure* 9(5):355-366.
798 27. Fowler SB, Best RB, Toca Herrera JL, Rutherford TJ, Steward A, Paci E, Karplus M,
799 & Clarke J (2002) Mechanical unfolding of a titin Ig domain: structure of unfolding
800 intermediate revealed by combining AFM, molecular dynamics simulations, NMR
801 and protein engineering. *J Mol Biol* 322(4):841-849.

28. Ismail N, Hedman R, Schiller N, & von Heijne G (2012) A biphasic pulling force acts on transmembrane helices during translocon-mediated membrane integration. *Nat Struct Mol Biol* 19(10):1018-1022.
29. Farias-Rico JA, Selin FR, Myronidi I, & Von Heijne G (2018) Effects of protein size, thermodynamic stability, and net charge on cotranslational folding on the ribosome. *bioRxiv*:303784.
30. Marino J, Heijne G, & Beckmann R (2016) Small protein domains fold inside the ribosome exit tunnel. *FEBS letters* 590(5):655-660.
31. Kramer G, Rauch T, Rist W, Vorderwulbecke S, Patzelt H, Schulze-Specking A, Ban N, Deuerling E, & Bukau B (2002) L23 protein functions as a chaperone docking site on the ribosome. *Nature* 419(6903):171-174.
32. Gong F & Yanofsky C (2003) A transcriptional pause synchronizes translation with transcription in the tryptophanase operon leader region. *J Bacteriol* 185(21):6472-6476.
33. Seidelt B, Innis CA, Wilson DN, Gartmann M, Armache JP, Villa E, Trabuco LG, Becker T, Mielke T, Schulten K, Steitz TA, & Beckmann R (2009) Structural insight into nascent polypeptide chain-mediated translational stalling. *Science* 326(5958):1412-1415.
34. Bischoff L, Berninghausen O, & Beckmann R (2014) Molecular basis for the ribosome functioning as an L-tryptophan sensor. *Cell Rep* 9(2):469-475.
35. Improta S, Politou AS, & Pastore A (1996) Immunoglobulin-like modules from titin I-band: extensible components of muscle elasticity. *Structure* 4(3):323-337.
36. Dunkle JA, Xiong L, Mankin AS, & Cate JH (2010) Structures of the Escherichia coli ribosome with antibiotics bound near the peptidyl transferase center explain spectra of drug action. *Proc Natl Acad Sci U S A* 107(40):17152-17157.
37. Karanicolas J & Brooks CL, 3rd (2003) Improved Go-like models demonstrate the robustness of protein folding mechanisms towards non-native interactions. *J Mol Biol* 334(2):309-325.
38. Karanicolas J & Brooks CL, 3rd (2003) The importance of explicit chain representation in protein folding models: an examination of Ising-like models. *Proteins* 53(3):740-747.
39. Karanicolas J & Brooks CL, 3rd (2003) The structural basis for biphasic kinetics in the folding of the WW domain from a formin-binding protein: lessons for protein design? *Proc Natl Acad Sci U S A* 100(7):3954-3959.
40. Elcock AH (2006) Molecular simulations of cotranslational protein folding: fragment stabilities, folding cooperativity, and trapping in the ribosome. *PLOS Comput Biol* 2(7):e98.
41. Muto H, Nakatogawa H, & Ito K (2006) Genetically encoded but nonpolypeptide prolyl-tRNA functions in the A site for SecM-mediated ribosomal stall. *Mol Cell* 22(4):545-552.
42. Bell GI (1978) Models for the specific adhesion of cells to cells. *Science* 200(4342):618-627.
43. Ferbitz L, Maier T, Patzelt H, Bukau B, Deuerling E, & Ban N (2004) Trigger factor in complex with the ribosome forms a molecular cradle for nascent proteins. *Nature* 431(7008):590.
44. Wild K, Halic M, Sinning I, & Beckmann R (2004) SRP meets the ribosome. *Nat Struct Mol Biol* 11(11):1049.
45. Frauenfeld J, Gumbart J, Van Der Sluis EO, Funes S, Gartmann M, Beatrix B, Mielke T, Berninghausen O, Becker T, & Schulten K (2011) Cryo-EM structure of the

ribosome–SecYE complex in the membrane environment. *Nat Struct Mol Biol* 18(5):614.

46. Best RB & Hummer G (2016) Microscopic interpretation of folding ϕ-values using the transition path ensemble. *Proc Natl Acad Sci U S A* 113(12):3263-3268.
47. Sánchez IE & Kiefhaber T (2003) Origin of unusual φ-values in protein folding: evidence against specific nucleation sites. *J Mol Biol* 334(5):1077-1085.
48. Best RB, Hummer G, & Eaton WA (2013) Native contacts determine protein folding mechanisms in atomistic simulations. *Proc Natl Acad Sci U S A* 110(44):17874-17879.
49. Best RB, Fowler SB, Herrera JL, Steward A, Paci E, & Clarke J (2003) Mechanical unfolding of a titin Ig domain: structure of transition state revealed by combining atomic force microscopy, protein engineering and molecular dynamics simulations. *J Mol Biol* 330(4):867-877.
50. Scott KA, Steward A, Fowler SB, & Clarke J (2002) Titin; a multidomain protein that behaves as the sum of its parts. *J Mol Biol* 315(4):819-829.
51. Williams PM, Fowler SB, Best RB, Toca-Herrera JL, Scott KA, Steward A, & Clarke J (2003) Hidden complexity in the mechanical properties of titin. *Nature* 422(6930):446-449.
52. Wright CF, Lindorff-Larsen K, Randles LG, & Clarke J (2003) Parallel protein-unfolding pathways revealed and mapped. *Nat Struct Biol* 10(8):658-662.
53. Wright CF, Steward A, & Clarke J (2004) Thermodynamic characterisation of two transition states along parallel protein folding pathways. *J Mol Biol* 338(3):445-451.
54. Borgia MB, Nickson AA, Clarke J, & Hounslow MJ (2013) A mechanistic model for amorphous protein aggregation of immunoglobulin-like domains. *J Am Chem Soc* 135(17):6456-6464.
55. Botello E, Harris NC, Sargent J, Chen WH, Lin KJ, & Kiang CH (2009) Temperature and chemical denaturant dependence of forced unfolding of titin I27. *J Phys Chem B* 113(31):10845-10848.
56. Chen H, Yuan G, Winardhi RS, Yao M, Popa I, Fernandez JM, & Yan J (2015) Dynamics of equilibrium folding and unfolding transitions of titin immunoglobulin domain under constant forces. *J Am Chem Soc* 137(10):3540-3546.
57. Lu H, Isralewitz B, Krammer A, Vogel V, & Schulten K (1998) Unfolding of titin immunoglobulin domains by steered molecular dynamics simulation. *Biophys J* 75(2):662-671.
58. Nunes JM, Mayer-Hartl M, Hartl FU, & Muller DJ (2015) Action of the Hsp70 chaperone system observed with single proteins. *Nat Commun* 6:6307.
59. Yagawa K, Yamano K, Oguro T, Maeda M, Sato T, Momose T, Kawano S, & Endo T (2010) Structural basis for unfolding pathway-dependent stability of proteins: vectorial unfolding versus global unfolding. *Protein Sci* 19(4):693-702.
60. Zheng W, Schafer NP, & Wolynes PG (2013) Frustration in the energy landscapes of multidomain protein misfolding. *Proceedings of the National Academy of Sciences* 110(5):1680-1685.
61. Carrion-Vazquez M, Oberhauser AF, Fowler SB, Marszalek PE, Broedel SE, Clarke J, & Fernandez JM (1999) Mechanical and chemical unfolding of a single protein: a comparison. *Proc Natl Acad Sci U S A* 96(7):3694-3699.
62. Su T, Cheng J, Sohmen D, Hedman R, Berninghausen O, von Heijne G, Wilson DN, & Beckmann R (2017) The force-sensing peptide VemP employs extreme compaction and secondary structure formation to induce ribosomal stalling. *eLife* 6:e25642.
63. Ziv G, Haran G, & Thirumalai D (2005) Ribosome exit tunnel can entropically stabilize α-helices. *Proc Natl Acad Sci U S A* 102(52):18956-18961.

64. Guinn EJ, Tian P, Shin M, Best RB, & Marqusee S (2018) A small single-domain protein folds through the same pathway on- and off- the ribosome. *bioRxiv*:347864.
65. Mercier E & Rodnina MV (2018) Co-translational Folding Trajectory of the HemK Helical Domain. *Biochemistry*.
66. Samelson AJ, Bolin E, Costello SM, Sharma AK, O'Brien EP, & Marqusee S (2018) Kinetic and structural comparison of a protein's cotranslational folding and refolding pathways. *Sci Adv* 4(5):eaas9098.
67. Evans MS, Sander IM, & Clark PL (2008) Cotranslational folding promotes β-helix formation and avoids aggregation in vivo. *J Mol Biol* 383(3):683-692.
68. Mirzadeh K, Martinez V, Toddo S, Guntur S, Herrgard MJ, Elofsson A, Norholm MH, & Daley DO (2015) Enhanced Protein Production in Escherichia coli by Optimization of Cloning Scars at the Vector-Coding Sequence Junction. *ACS Synth Biol* 4(9):959-965.
69. Li X, Mooney P, Zheng S, Booth CR, Braunfeld MB, Gubbens S, Agard DA, & Cheng Y (2013) Electron counting and beam-induced motion correction enable near-atomic-resolution single-particle cryo-EM. *Nat Methods* 10(6):584-590.
70. Scheres SH (2012) RELION: implementation of a Bayesian approach to cryo-EM structure determination. *J Struct Biol* 180(3):519-530.
71. Zhang K (2016) Gctf: Real-time CTF determination and correction. *J Struct Biol* 193(1):1-12.
72. Kucukelbir A, Sigworth FJ, & Tagare HD (2014) Quantifying the local resolution of cryo-EM density maps. *Nat Methods* 11(1):63-65.
73. Pettersen EF, Goddard TD, Huang CC, Couch GS, Greenblatt DM, Meng EC, & Ferrin TE (2004) UCSF Chimera--a visualization system for exploratory research and analysis. *J Comput Chem* 25(13):1605-1612.
74. Hess B, Kutzner C, Van Der Spoel D, & Lindahl E (2008) GROMACS 4: algorithms for highly efficient, load-balanced, and scalable molecular simulation. *J Chem Theory and Comput* 4(3):435-447.
75. Hess B, Bekker H, Berendsen HJ, & Fraaije JG (1997) LINCS: a linear constraint solver for molecular simulations. *J Comput Chem* 18(12):1463-1472.
76. Sirur A, Knott M, & Best RB (2014) Effect of interactions with the chaperonin cavity on protein folding and misfolding. *Phys Chem Chem Phys* 16(14):6358-6366.
77. Bortz AB, Kalos MH, & Lebowitz JL (1975) A new algorithm for Monte Carlo simulation of Ising spin systems. *J Comput Phys* 17(1):10-18.
78. Öhman A, Öman T, & Oliveberg M (2010) Solution structures and backbone dynamics of the ribosomal protein S6 and its permutant P54-55. *Protein Sci* 19(1):183-189.
79. Pascual J, Pfuhl M, Walther D, Saraste M, & Nilges M (1997) Solution structure of the spectrin repeat: a left-handed antiparallel triple-helical coiled-coil1. *J Mol Biol* 273(3):740-751.

## Supplementary Figures

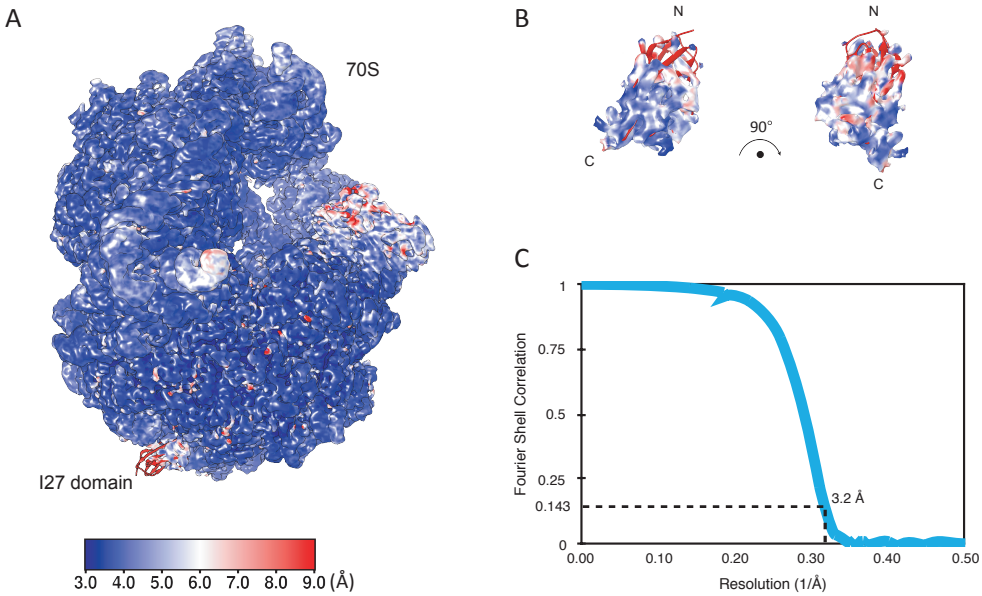


**Figure S1.** Resolution of the ribosome-nascent chain complex (RNC). (A) Calculation of the local resolution using Resmap (Kucukelbir, A. et al. Nat Methods 11, 63-65, 2014). The RNC density is displayed at 1.7 RMSD. (B) local resolution of the I27 domain. The I27 domain density is displayed at 2 RMSD. N and C termini are indicated. (C) Fourier-shell correlation (FSC) curve of the refined final map of the RNC, indicating the average resolution of 3.2 Å (at 0.143).

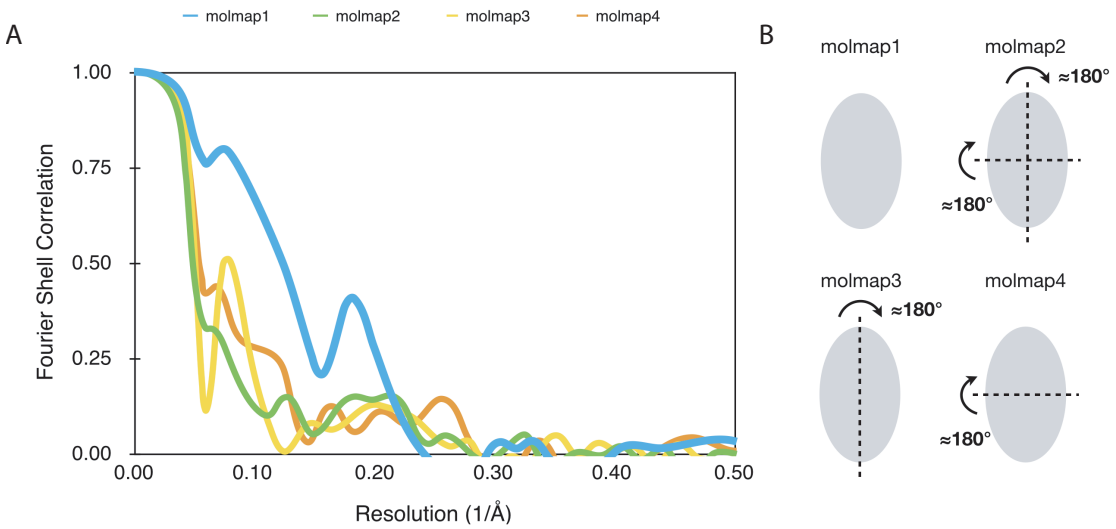


**Figure S2.** Validation of model orientation for I27 domain. To validate the orientation of the I27 domain model (PDB 1TIT) to its corresponding density, four possible orientations were tested. (A) The Fourier-shell correlations between the isolated I27 density and the map generated from the model of the final orientation (molmap1, blue) and the models fitted with the other three possibilities (molmap2, green; molmap3, yellow; molmap4, orange) were plotted. In the frequency range 0 to 0.2 (1000 to 5 Å) the correlation of molmap1 is significantly higher compared to all other orientation molmaps. (B) The illustration showing the relationship among the four model orientations. Since the density represents a flat ellipsoid, we used all four major and minor axes covering all possible orientations of the model fitting within the density.

967

968

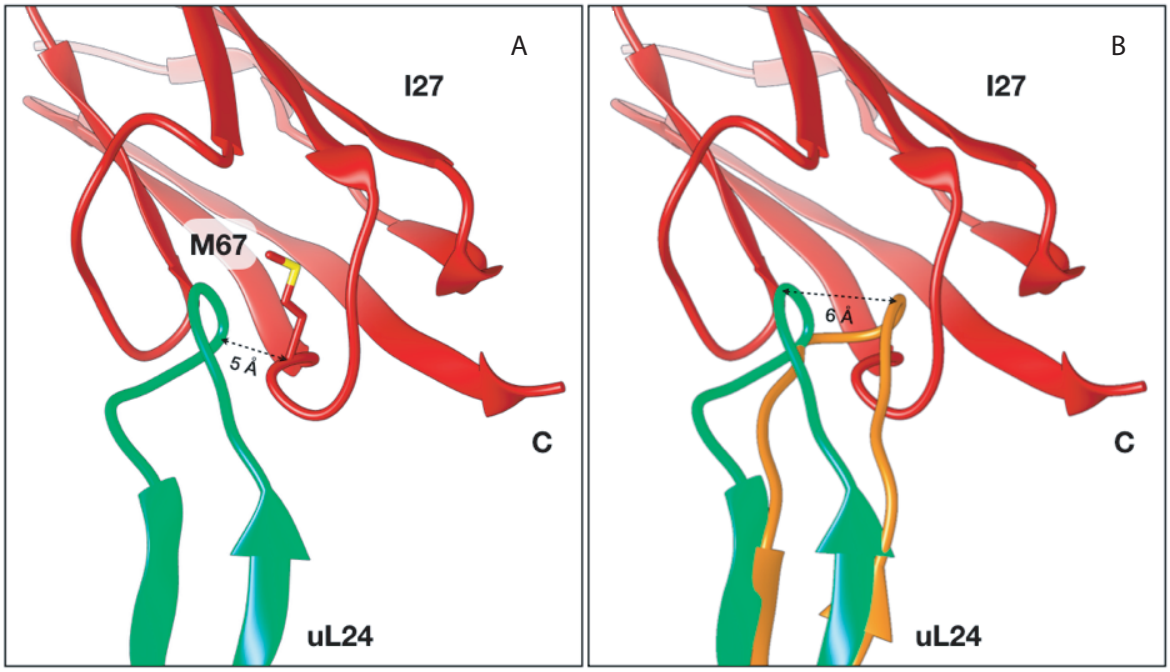


969

970 **Figure S3.** The I27 domain and a β hairpin in ribosomal protein uL24 close to the ribosomal
971 exit tunnel. (A) Residue M67 in the I27 domain is located in close proximity to a β hairpin
972 loop in uL24 in the cryo-EM structure of I27-TnaC[*L*=35] RNCs. (B) The uL24 β hairpin in
973 the I27-RNC (light green; re-modeled based on PDB 5NWY) is ~ 6 Å shifted (distance
974 measured via the backbone of Pro50) compared to its location in the VemP-RNC (orange;
975 PDB 5NWY) and the TnaC-RNC (PDB 4UY8, not shown). C represents the C terminus of
976 the I27 domain.

977

978

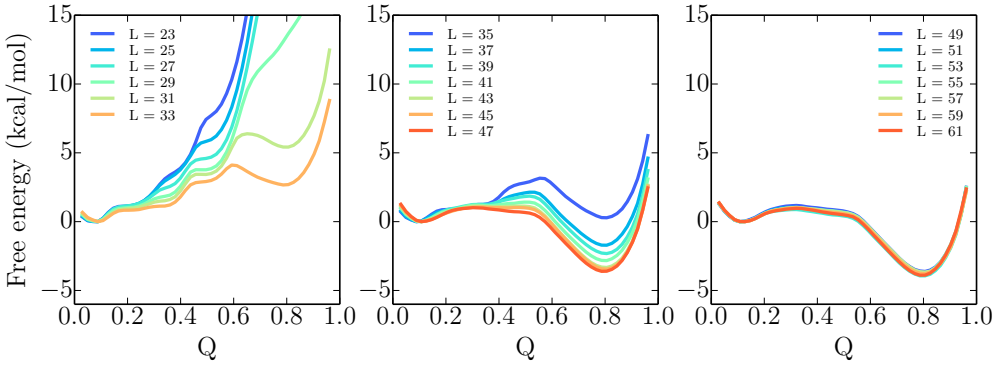


**Figure S4**. Simulation free energy $F(Q)$ projected on the fraction of native contacts, $Q$, for I27 folding with different linker lengths (as indicated in legend) at 291K.

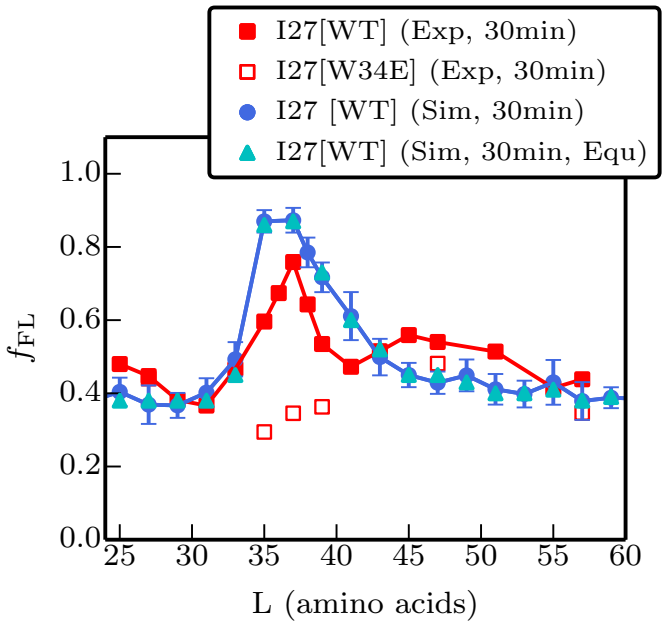


**Figure S5.** Experimental (red) and simulated profiles of fraction full length protein, $f_{FL}$, obtained with a 30 min incubation. Note the higher background values compared to main text Figures 1 and 3D. Force profiles calculated from simulations using full kinetic scheme and pre-equilibrium model are shown in blue circles and cyan triangles respectively. The RMSD of the $f_{FL}$ between experiment and simulation is 0.12.

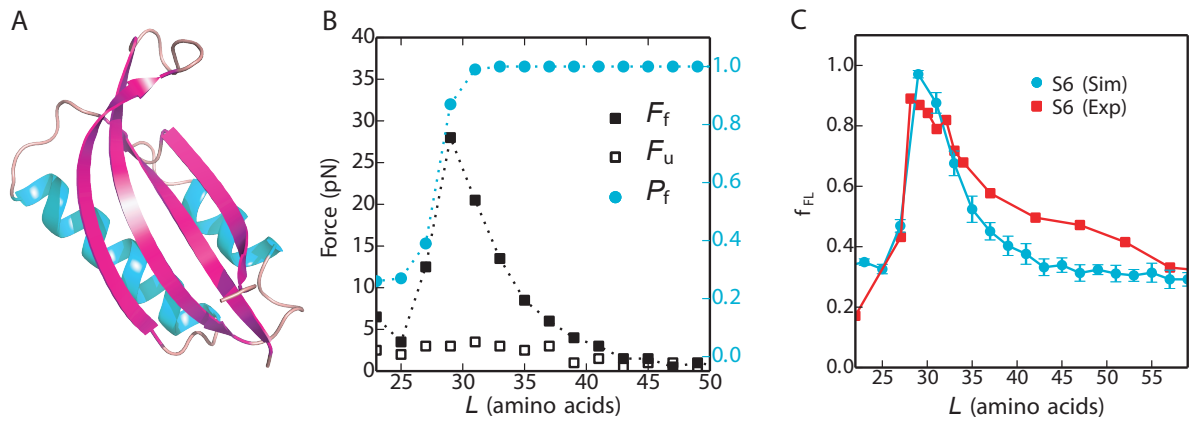


**Figure S6**. (A) Native structure of protein S6 (pdb code: 2KJV (78)) B) Average forces exerted on the AP by the unfolded state ($F_f$ , filled black symbols) and folded state ($F_u$ , empty black symbols) of S6 at different linker lengths *L*. The average fraction folded S6 for different *L*, $P_f$, is shown in cyan on the right axis. (C) Experimental (red) and simulated (cyan) force profiles for cotranslational folding of S6 based on pre-equilibrium kinetic solution.

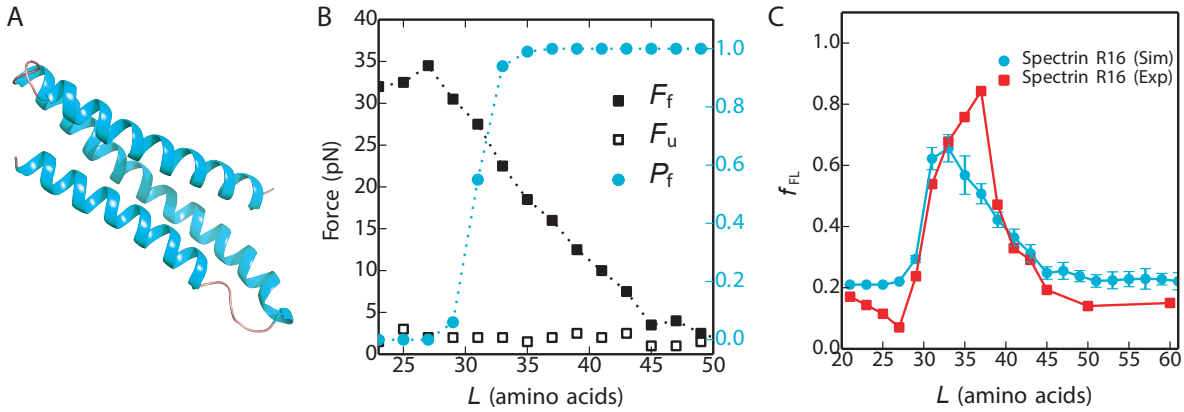


**Figure S7**. (A) Native structure of Spectrin R16 domain (PDB 1AJ3 (79)). (B) Average forces exerted on the AP by the unfolded state ($F_f$, empty black symbols) and folded state ($F_u$, filled black symbols) of R16 at different linker lengths L. The average fraction folded R16 for different L, $P_f$, is shown in cyan on the right axis. (C) Experimental (red) and simulated (cyan) force profiles for cotranslational folding of R16 based on the pre-equilibrium kinetic solution.

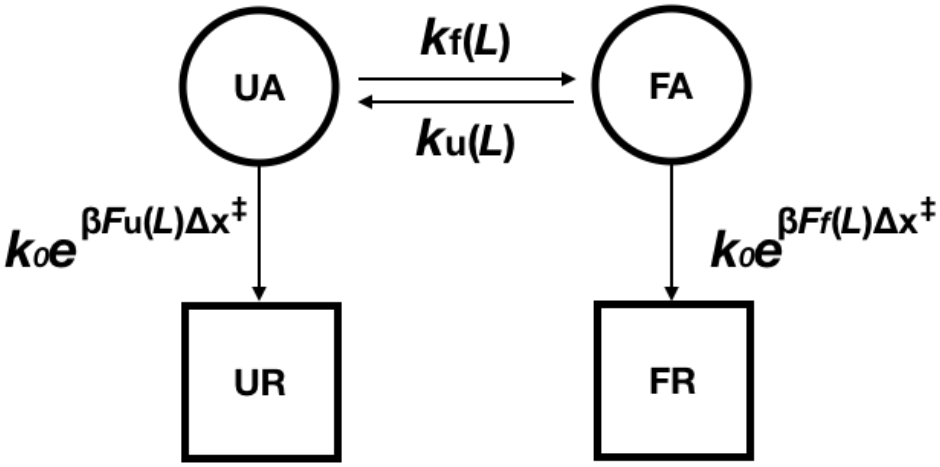


**Figure S8.** Schematic for the full kinetic model which describes the escape pathway of I27 from the ribosome. $k_f$ and $k_u$ are the linker length-dependent folding and unfolding rates respectively. UA: I27 is unfolded and arrested by ribosome. FA: I27 is folded and arrested by ribosome. UR: I27 is unfolded and released from ribosome. FR: I27 is folded and released from ribosome.

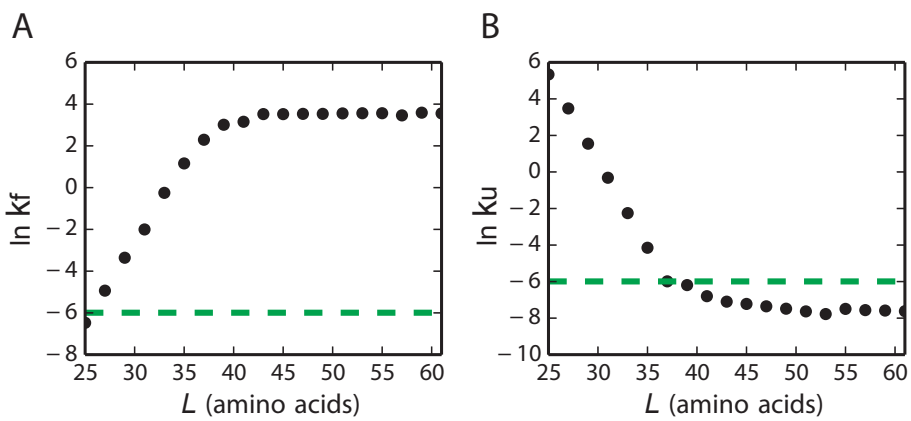


**Figure S9.** Dependence of folding rate $k_f$ (left) and unfolding rate $k_u$ (right) on the length of the linker between the AP and I27. Rates determined directly from simulations have been scaled so that $k_f$ and $k_u$ at large linker lengths are equal to the experimental values determined for the isolated protein. The green dashed line indicate the force-dependent escape rate of ~ 2.4 x $10^{-3}$ $s^{-1}$ obtained at the force of 20 pN.

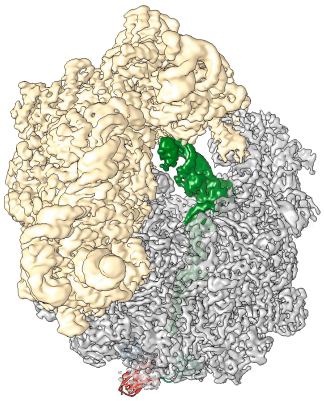

**Supporting Video S1**. Cryo-EM density of ribosome and I27 (one static frame of the video). Video showing cryo-EM map for I27[L=35] RNCs. 30S in yellow, 50S and I27 domain in grey, tRNA and nascent chain in green, the model (PDB 1TIT) of I27 domain in red.

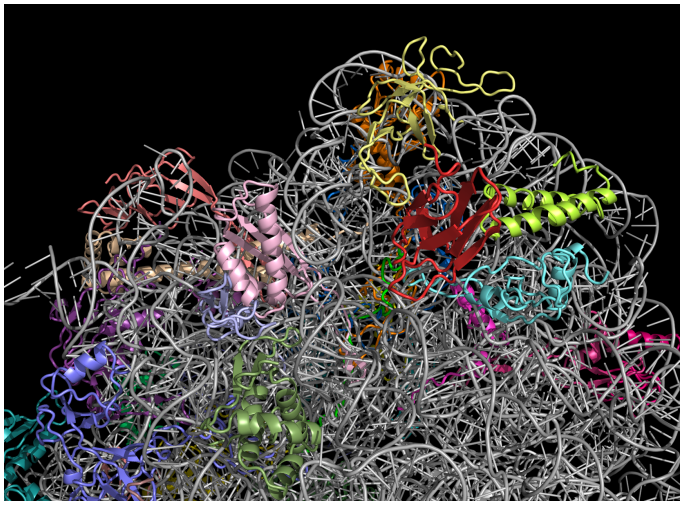

**Supporting Video S2.** MD folding simulation (one static frame of the video). Video showing an unbiased 1.8 μsec fragment of an MD trajectory of I27 folding and unfolding at linker length *L*=35. Ribosomal 23s rRNA is shown in white cartoon mode, ribosomal proteins uL24, uL29, uL23 are shown in yellow, lime and cyan respectively. I27 and linker are in red and green cartoon mode respectively.